Large-scale exact diagonalizations reveal low-momentum scales of nuclei

Downloaded from: https://research.chalmers.se, 2025-12-05 01:47 UTC

Citation for the original published paper (version of record):
Forssen, C., Karlsson, B., Johansson, H. et al (2018). Large-scale exact diagonalizations reveal low-momentum scales of nuclei. Physical Review C, 97(3).
http://dx.doi.org/10.1103/PhysRevC.97.034328

N.B. When citing this work, cite the original published paper.

research.chalmers.se offers the possibility of retrieving research publications produced at Chalmers University of Technology. It covers all kind of research output: articles, dissertations, conference papers, reports etc. since 2004. research.chalmers.se is administrated and maintained by Chalmers Library

(article starts on next page)

Large-scale exact diagonalizations reveal low-momentum scales of nuclei

C. Forssén,* B. D. Carlsson, H. T. Johansson, and D. Sääf
Department of Physics, Chalmers University of Technology, SE-412 96 Göteborg, Sweden

A. Bansal, G. Hagen, and T. Papenbrock
Department of Physics and Astronomy, University of Tennessee, Knoxville, Tennessee 37996, USA
and Physics Division, Oak Ridge National Laboratory, Oak Ridge, Tennessee 37831, USA

(Received 8 January 2018; published 28 March 2018)

Ab initio methods aim to solve the nuclear many-body problem with controlled approximations. Virtually exact numerical solutions for realistic interactions can only be obtained for certain special cases such as few-nucleon systems. Here we extend the reach of exact diagonalization methods to handle model spaces with dimension exceeding 10^{10} on a single compute node. This allows us to perform no-core shell model (NCSM) calculations for ^{6}Li in model spaces up to $N_{\max} = 22$ and to reveal the ^{4}He+d halo structure of this nucleus. Still, the use of a finite harmonic-oscillator basis implies truncations in both infrared (IR) and ultraviolet (UV) length scales. These truncations impose finite-size corrections on observables computed in this basis. We perform IR extrapolations of energies and radii computed in the NCSM and with the coupled-cluster method at several fixed UV cutoffs. It is shown that this strategy enables information gain also from data that is not fully UV converged. IR extrapolations improve the accuracy of relevant bound-state observables for a range of UV cutoffs, thus making them profitable tools. We relate the momentum scale that governs the exponential IR convergence to the threshold energy for the first open decay channel. Using large-scale NCSM calculations we numerically verify this small-momentum scale of finite nuclei.

DOI: 10.1103/PhysRevC.97.034328

I. INTRODUCTION

The harmonic-oscillator basis continues to be most popular in the computation of atomic nuclei. It is employed in the traditional shell model [1–3], nuclear density functional calculations [4–6], the no-core shell model (NCSM) [7,8], and other *ab initio* methods [9–11]. For such *ab initio* approaches, one usually employs a very large basis including many orbitals. This serves two simultaneous purposes: (i) the basis should capture the correlations induced by the strong, realistic nucleon-nucleon interactions that are used as input, and (ii) it should build the long-range behavior of nuclear wave functions and possibly incorporate effects of continuum coupling [12]. Still, the basis must obviously be truncated and one might ask the relevant question: What are the corrections to energies and other observables that are due to the finite size of the oscillator basis?

This question was addressed in several works by empirical extrapolation schemes [13–17]. Only recently—based on the insight that a finite oscillator space introduces IR and UV cutoffs [18–21]—were extrapolation formulas derived for the harmonic-oscillator basis. The IR extrapolation formulas [22] are the harmonic-oscillator equivalent of Lüscher's formula for the lattice [23]. The key insight was that the spherical harmonic-oscillator basis is—at low energies—indistinguishable from a spherical cavity of radius L. As the Lüscher formula corrects the energy shift from tunneling due to the periodic boundary condition of the underlying lattice, the IR extrapolation formulas correct the energy shift due to the Dirichlet boundary condition at the radius L. Very recently, high-precision expressions for the length scale L were derived for the two-body problem [24], many-body spaces that are products of single-particle spaces [25], and the NCSM [26] in which a total energy truncation is employed. Extrapolation formulas were derived for energies [22], radii [24], quadrupole transitions [27], and radiative capture reactions [28]. For finite-volume corrections to the binding energy of N-particle quantum bound states on the lattice we refer the reader to Ref. [29].

The leading-order (LO) IR extrapolation formula for energies is

$$E(L) = E_\infty + a_0 \exp(-2k_\infty L). \tag{1}$$

The energies $E(L)$ are theoretical results for bound-state energies, while a_0 and k_∞ are adjustable parameters that are so far only understood in the two-body problem [24]. The IR extrapolation Eq. (1) reflects that a finite oscillator basis effectively imposes a hard-wall boundary condition at a radius L. Thus, $a_0 > 0$ and the computed energies $E(L)$ are above the infinite space result E_∞. The extrapolation formula Eq. (1) is expected to yield an accurate bound-state energy when UV convergence is already achieved, and when L significantly exceeds any other relevant length scale, i.e., for $k_\infty L \to \infty$. For the deuteron, subleading corrections (in $k_\infty L$) to Eq. (1) are also known [30]. We note that UV extrapolations of bound-state energies are more challenging than IR extrapolations

*christian.forssen@chalmers.se

 ©2018 American Physical Society

because the former depend on the regulators and short-range details of the employed interactions [31], while the latter are insensitive to such details.

In practice, it is often challenging to fulfill the two conditions (i.e., being both UV converged and working at asymptotically large values of $k_\infty L$), and it would be profitable to relax these conditions. We also note that IR extrapolations of bound-state energies—when performed at large UV cutoffs that significantly exceed the cutoff of the employed interaction—sometimes fail to improve on the variational minimum; see Refs. [25,26] for examples. This casts some doubts on the usefulness of such extrapolations and makes it necessary to revisit them in more detail. The development of a practical and reliable scheme for IR extrapolations is a specific purpose of this paper.

While the NCSM method promises many-body results without any uncontrolled approximations, it often faces computational limits in terms of both CPU and memory requirements. A second objective of our work is to push the limit of the exact-diagonalization method in nuclear physics. This extended reach will make it possible to probe how numerical results depend on UV and IR scales. In particular, we will see that the separation momentum of the lowest-lying decay channel is the relevant low-momentum scale of bound states in finite nuclei. An improved understanding of IR extrapolation can be employed to optimize the choice of model-space parameters so that the information yield of costly many-body calculations is maximized.

This paper is organized as follows: In Sec. II we propose IR extrapolation formulas for energies and radii that are applicable in cases lacking a full UV convergence. The extended reach of large-scale exact diagonalization with the NCSM is presented in Sec. III, with more details on the technical developments that have made such calculations possible adjourned to the Appendix A. We then present an extensive set of large-basis NCSM results and apply the IR extrapolation formulas to several s- and p-shell nuclei in Secs. IV and V, respectively. We also present results from coupled-cluster computations. We summarize our results in Sec. VI.

II. DERIVATION

Let us assume we work in model spaces with a fixed value of Λ—the UV momentum cutoff scale—that is not yet so large that UV convergence is fully achieved. Usually this is the case for values of Λ that only moderately exceed the cutoff employed by the interaction. As the IR length L is increased, the tail of the bound-state wave function will be built up, and we see that Eq. (1) at fixed Λ generalizes to

$$E(L,\Lambda) = E_\infty(\Lambda) + a_0(\Lambda)\exp[-2k_\infty(\Lambda)L]. \quad (2)$$

Equation (2) is only the leading term for asymptotically large $k_\infty L$ but exhibits the full Λ dependence [at least for Λ large enough to yield a bound-state energy $E(L,\Lambda)$]. We note that the combined IR and UV extrapolation formula applied in Ref. [22] is a special case of Eq. (2) with constant k_∞, a_0 and $E_\infty(\Lambda) = E_\infty + A_0\exp(-2\Lambda^2/A_1^2)$.

Let us discuss subleading corrections to Eq. (2). Contributions of partial waves with finite angular momentum lead to corrections proportional to

$$\sigma_{\rm IR} = \frac{\exp[-2k_\infty(\Lambda)L]}{k_\infty(\Lambda)L}. \quad (3)$$

Even smaller corrections are of order $\exp(-4k_\infty L)$. So far, little is known about corrections in nuclei consisting of three or more nucleons. Below we will argue that k_∞ is the momentum to the first open separation channel (or particle-emission channel). In nuclei with several open channels (e.g., separation of neutrons, of protons, or of α particles), the leading corrections from each channel are expected to be on the order of $\exp[-2k_{\rm sep}(i)L]$, where $k_{\rm sep}(i)$ is the separation momentum of channel i. Such corrections could be sizable for particle emission channels with similar energy thresholds and/or with sizable asymptotic normalization coefficients (ANCs) [29,32].

Let us consider applications of the extrapolation Eq. (2) at fixed Λ. In the harmonic-oscillator basis, the oscillator length is

$$b \equiv \sqrt{\frac{\hbar}{m\omega}} \quad (4)$$

for a nucleon mass m and the oscillator frequency ω. The IR length scale L and the UV cutoff Λ are related to each other [31],

$$\begin{aligned} L(N,b) &= f(N)b, \\ \Lambda(N,b) &= f(N)\hbar b^{-1}, \end{aligned} \quad (5)$$

because of the complementarity of momenta and coordinates. Here, $f(N)$ is a function that depends on the number N of quanta that can be excited. This function also depends on the number of particles and differs for product spaces and NCSM spaces. We will use the standard notation $N_{\rm max}$ to denote an NCSM truncation of $N_{\rm max}$ quanta above the lowest possible configuration. The maximum number of quanta for a single particle in such a basis will be, e.g., $N = N_{\rm max} + 1$ for a p-shell nucleus. Following More *et al.* [24], $f(N) \approx [2(N + 3/2 + 2)]^{1/2}$ when $N \gg 1$ for a two-body system in the center-of-mass frame. In general, $f(N) \propto N^{1/2}$ for $N \gg 1$ [26,30].

We can express L in Eq. (5) as $L(N,\Lambda) = \hbar f^2(N)/\Lambda$. Thus, $L \propto N$ for $N \gg 1$ at fixed Λ. This shows that IR extrapolations Eq. (2) at fixed Λ are actually exponential in N. Formally, this result coincides with several commonly used extrapolation formulas [13–17,33]. We also note that this result agrees with semiclassical arguments regarding the convergence of bound states in the harmonic-oscillator basis [34].

For radii, we proceed as for the bound-state energies and generalize the extrapolation formulas of Refs. [22,30] to

$$r^2(L,\Lambda) = r^2_\infty(\Lambda) - \alpha(\Lambda)[k_\infty(\Lambda)L]^3\exp[-2k_\infty(\Lambda)L] \quad (6)$$

at fixed UV cutoff Λ. Here, corrections are of the size

$$\sigma_{r,\rm IR} = [k_\infty(\Lambda)L]\exp[-2k_\infty(\Lambda)L] \quad (7)$$

for the two-body bound state. As for the energies, there are other radius corrections in nuclei consisting of three or more nucleons. For these reasons, we will employ only the leading corrections, i.e., Eq. (2) for the energies and Eq. (6) for radii in extrapolations of data. In the corresponding χ^2 fits, we

will employ the uncertainties scaled with Eqs. (3) and (7), respectively.

In the extrapolation Eqs. (2) and (6), the Λ-dependent quantities are taken as adjustable parameters. In the deuteron, k_∞ and a_0 are related to the binding energy B and the ANC via [30]

$$B = \frac{\hbar^2 k_\infty^2}{2\mu}, \tag{8}$$

$$\gamma_\infty^2 = \frac{\mu a_0}{\hbar^2 k_\infty}. \tag{9}$$

Here, $\mu = m/2$ is the reduced mass, k_∞ is the separation momentum, and γ_∞ is the ANC defined by large-r behavior of the deuteron wave function in the relative coordinate $\vec{r} = \vec{r}_1 - \vec{r}_2$. We note that the oscillator length for this coordinate employs the reduced mass instead of the nucleon mass in Eq. (4). Below, we will employ length and momentum scales that are based on Eq. (4).

We would like to understand the physics meaning of k_∞ in IR extrapolations of NCSM results for few- and many-body systems. For many-body bound states on a cubic lattice, this parameter was very recently identified with the separation momentum [29]. In what follows we arrive at a similar identification for the harmonic-oscillator basis of the NCSM. In the NCSM, the IR length Eq. (5) constitutes an effective hard wall for the hyperradius ρ with

$$\vec{\rho}^{\,2} = \sum_{j=1}^{A} \vec{r}_i^{\,2} - A\vec{R}_{\rm cm}^{\,2}, \tag{10}$$

where

$$\vec{R}_{\rm cm} \equiv \frac{1}{A}\sum_{j=1}^{A} \vec{r}_j \tag{11}$$

is the center of mass coordinate. We use an orthogonal transformation and introduce Jacobi coordinates $\vec{\rho}_1, \ldots, \vec{\rho}_A$ such that

$$\vec{\rho}_A = A^{1/2}\vec{R}_{\rm cm} = \frac{1}{\sqrt{A}}\sum_{j=1}^{A} \vec{r}_j. \tag{12}$$

Using an orthogonal transformation has the advantage that the reduced mass corresponding to each of the Jacobi coordinates is simply the nucleon mass m. Thus, the oscillator length for each Jacobi coordinate is given by Eq. (4).

We note that there are many ways to introduce Jacobi coordinates $\vec{\rho}_1$ to $\vec{\rho}_{A-1}$ that are orthogonal to each other and orthogonal to $\vec{\rho}_A$ in Eq. (12). In particular, one can choose $\vec{\rho}_1$ such that it corresponds to the lowest-energetic separation channel. See, for example, the illustrations in Fig. 1, where $\vec{\rho}_1 = (\vec{r}_2 - \vec{r}_1)/\sqrt{2}$ for the deuteron, $\vec{\rho}_1 = [\vec{r}_3 - (\vec{r}_1 + \vec{r}_2)/2]\sqrt{2/3}$ for the triton (because its lowest separation is into a neutron and a deuteron), and $\vec{\rho}_1 = [(\vec{r}_5 + \vec{r}_6)/2 - (\vec{r}_1 + \vec{r}_2 + \vec{r}_3 + \vec{r}_4)/4]\sqrt{4/3}$ for ^{6}Li (because its lowest separation threshold is into an alpha particle and the deuteron). Here, we limit ourselves to breakup into two clusters. For any orthogonal choice of Jacobi coordinates, the intrinsic hyperradius is

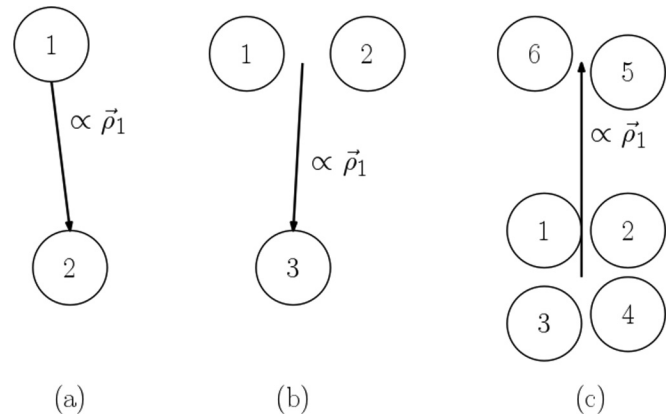

FIG. 1. Choice of Jacobi coordinates for the deuteron (a), the triton (b), and ^{6}Li (c) such that $\vec{\rho}_1$ corresponds to the channel with the lowest separation energy.

$$\rho^2 = \sum_{j=1}^{A-1} \rho_j^2. \tag{13}$$

We note that the effective hard-wall radius L of the NCSM [26] constitutes a hard-wall boundary condition also for the Jacobi coordinate $\vec{\rho}_1$. Thus, bound-state wave functions in this coordinate fall off asymptotically as $e^{-k_1\rho_1}$, with $\vec{k}_1$ being the momentum conjugate to $\vec{\rho}_1$. We denote $k_1 \equiv k_{\rm sep}$ as the separation momentum, with the corresponding separation energy,

$$S = \frac{\hbar^2 k_{\rm sep}^2}{2m}, \tag{14}$$

where m is the nucleon mass. We note that this mass (opposed to a reduced mass) enters here, because we used an orthogonal transformation from $(\vec{r}_1, \ldots, \vec{r}_A)$ to the Jacobi coordinates.

As the IR extrapolation Eq. (2) is based on the exponential falloff $\sim\exp(-k_\infty\rho_1)$ of bound-state wave functions in position space, we now identify

$$k_\infty = k_{\rm sep}, \tag{15}$$

with the separation energy $S_\infty = \hbar^2 k_\infty^2/(2m)$. Based on the derivation in Appendix C and Ref. [29], we also identify

$$a_0 = \frac{\hbar^2 k_{\rm sep}\gamma_{\rm sep}^2}{m}, \tag{16}$$

where $\gamma_{\rm sep}$ is the ANC corresponding to the Jacobi coordinate ρ_1. Taking the different choice of coordinates into account, we note that Eqs. (14)–(16) yield the same value for the separation energy Eq. (8) in case of the two-body bound state [30].

We recall that the relation Eq. (15) between the momentum of the lowest separation channel and the fit parameter k_∞ from IR extrapolations in the NCSM is valid only in the asymptotic regime $k_\infty L \to \infty$. Many nuclei exhibit n different separation channels, with proton, neutron, and alpha-particle separation usually being among the least energetic ones. These channels can correspond to different orthogonal Jacobi coordinates or also to different choices of Jacobi coordinates (that are not

orthogonal to each other). In any case, the corresponding momenta $k_1 \leqslant k_2 \leqslant \cdots \leqslant k_n$ might not be well separated in scale. In practical NCSM calculations, one can only reach the regime $k_1 L \gg 1$, and this means that other separation channels can yield non-negligible corrections to the leading-order IR extrapolation Eqs. (2) and (6). In those cases, IR extrapolation will only yield an approximate value for $k_{\rm sep}$, and the application of Eqs. (14) and (15) will only yield an approximate value for the separation energy.

In Secs. IV and V we apply the extrapolation Eqs. (2) and (6) to obtain bound-state energies and radii at fixed Λ for different s- and p-shell nuclei, respectively. We use the nucleon-nucleon interaction NNLO$_{\rm opt}$ [35] with a regulator cutoff $\Lambda_\chi = 500$ MeV. The nuclei ^{3}H, ^{3}He, and ^{4}He will serve as examples where the IR extrapolation scheme and the interpretation of the results can be validated by also performing converged NCSM calculations. We will then study several p-shell systems: ^{6}Li, ^{6,8}He, and ^{16}O. For ^{8}He we benchmark IR extrapolated results at fixed Λ from the NCSM and the coupled-cluster method (CC) [10] while we use only the CC method for ^{16}O.

III. EXACT DIAGONALIZATION WITH THE NCSM

The NCSM approach employed in this work has been described in several papers; see, e.g., Refs. [7,8]. The main feature of this *ab initio* method is the use of the harmonic-oscillator basis, truncated by a chosen maximal total oscillator energy of the A-nucleon system as defined by the model-space parameter $N_{\rm max}$. The Hamiltonian matrix is constructed in this basis and the relevant eigensolutions are typically found using iterative diagonalization methods.

In the NCSM approach one does not make any approximations concerning the structure of the many-body wave function. Therefore, the method can, in principle, describe any kind of (bound) many-body state; although the convergence might be slow in some cases, e.g., for systems that exhibit a large degree of clusterization or very low separation thresholds. The main disadvantage of this method is the rapid growth in model-space size with the number of particles and $N_{\rm max}$ truncation. In many NCSM studies one employs basis-dependent unitary transformations to speed up convergence. In this work, however, we use bare nuclear interactions.

We discuss the frontier of NCSM calculations in terms of model-space dimension and matrix sizes in the next subsection, before describing the NCSM code `pANTOINE` that has been used in this work.

A. Pushing the frontier of exact diagonalization

Let us use ^{6}Li as an example of NCSM dimensions and matrix sizes. The M-scheme ($M = 1$) model space dimension as a function of $N_{\rm max}$ is shown on a semilogarithmic scale in the upper panel of Fig. 2. We note that 64-bit indices are needed when the dimension exceeds 4.2×10^9 (for ^{6}Li this occurs at $N_{\rm max} = 20$). For such dimensions it also becomes difficult to fit the full vector in the machine memory.

However, the number of nonzero matrix elements, and the corresponding number of operations needed for matrix-vector multiplications, is the most restricting factor for these calculations. Restricting ourselves to two-body interactions, the number of nonzero matrix elements for ^{6}Li is shown in the lower panel of Fig. 2. The data for this figure is generated employing the symmetry of the Hamiltonian matrix, counting only matrix elements in the upper half of the matrix. A staggering amount of 2 PB memory storage space would be required for the $N_{\rm max} = 22$ calculations assuming that we would explicitly store the matrix using double precision. In order to provide a relevant perspective on this number we note that the most memory given for a machine on the current TOP500 list is 1.6 PB [36]. Obviously, the inclusion of three-body interaction terms would make this problem even more dramatic.

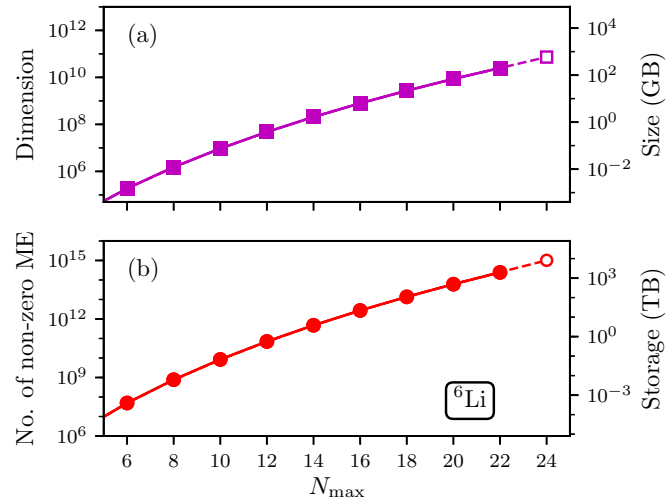

FIG. 2. Scaling plots for the ^{6}Li nuclear many-body problem ($M = 1$) as a function of the NCSM model space truncation $N_{\rm max}$. (a) Model space dimension; (b) Number of nonzero matrix elements (with two-body interactions only). The right axes displays the corresponding size (in TB) assuming that the elements are explicitly stored in double-precision floating-point format. Extrapolated data is shown as open symbols.

Let us also comment on the efficiency limit for performing the matrix-vector multiplications that are needed for iterative diagonalization methods. While an explicit-matrix code likely can perform 1 multiplication (mult) per clock cycle in each core, a more restrictive limit will be given by the memory bandwidth. Assume the elements are organized such that the vector data resides in processor cache and thus memory bandwidth can be fully utilized to load indices and matrix data. Each element processed corresponds to about 10 bytes loaded, in a streaming fashion. State-of-the art server CPUs have eight channels of DDR4 memory that can deliver just over 20 GB/s, and thus sustain 16 Gmult/s per socket. At the same time, such server CPUs may have 32 cores running at 2.7 GHz, giving 86.4G clock cycles/s. Memory bandwidth thus limits the performed multiplications to 0.2 per clock cycle. Utilizing the symmetry of the Hamiltonian matrix, this becomes 0.4 mult/clock cycle. This number constitutes an important performance benchmark for exact diagonalization codes.

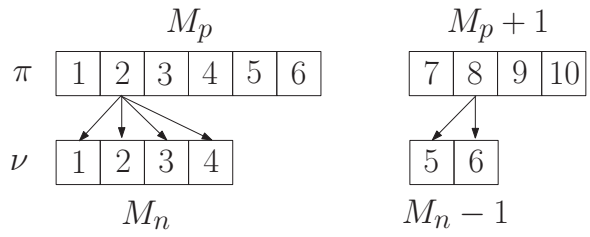

FIG. 3. Many-body states in the proton and neutron sub-spaces factorize into blocks according to their J_z projection. A-particle states with fixed $J_z = M$ are product states $|I\rangle = |\pi\rangle \otimes |\nu\rangle$ with proton- and neutron states from corresponding blocks.

A possible solution to overcome the memory size limit is the implicit (re-)construction of matrix elements rather than explicit storage. In the next section we briefly discuss the sophisticated shell-model and NCSM code pANTOINE that is designed to achieve just that. We note that similar factorization techniques are used in the configuration-interaction code BIGSTICK [37]. Unavoidably, the bookkeeping that is needed to accomplish the reconstruction of the matrix will lower the efficiency of the calculations. We will show in Appendix A that careful code design can limit this extra cost to about a factor four in reduced efficiency.

B. Exact diagonalization with implicit matrix construction

The $A > 4$ NCSM calculations presented in this work have been performed with pANTOINE—an exact diagonalization code for nuclear physics that is based on the NCSM version of ANTOINE originally developed by Caurier and coworkers [38–40]. The main feature of this code is the implicit construction of the Hamiltonian matrix, implying on-the-fly computation of matrix elements in the iterative matrix-vector multiplications. It employs the fact that the total many-body space is a product of the much smaller spaces spanned by protons and neutrons separately. A state I in the full-space basis can be labeled by a pair of proton (π) and neutron (ν) states in the subspace bases, as illustrated in Fig. 3. All the π (and ν) states are divided into blocks defined by their J_z value. To any proton block $J_{z,p} = M_p$ there is a corresponding neutron block $J_{z,n} = M_n = M - M_p$, where $J_z = M$ is the total angular momentum projection of the A-body state. The full many-body basis is built by the association of proton states π (belonging to the block M_p) with neutron states ν (belonging to the corresponding neutron block M_n). A simple numerical relation,

$$I = R(\pi) + \nu, \tag{17}$$

describing the index of a full multiparticle state can be established. Nonzero elements of the matrix, $H_{II'} = V(K)$, are obtained through three integer additions: $I = R(\pi) + \nu$, $I' = R(\pi') + \nu'$ and $K = Q(q_\pi) + q_\nu$. The index q_π labels the one-body operator acting between π and π' states, and analogously the index q_ν links ν and ν' states. The storage of precalculated (π,π',q_π) and (ν,ν',q_ν) labels remains possible as the dimensions in respective proton- and neutron-spaces are moderate compared to those of the full A-body space. Note that each triple either applies to the proton- or neutron-subspace only. By performing a double-loop over the pairs of such triple-lists, and performing the index additions, all connections in the matrix can be efficiently processed.

With pANTOINE we have introduced several improvements of the ANTOINE code and managed to significantly push the frontier of exact diagonalization methods for few and many-nucleon systems. In particular, we have achieved to extend six-body (^{6}Li) NCSM calculations with two-body interactions from $N_{\max} = 18$, which was the previous computational limit [26,41], to $N_{\max} = 22$. This translates to an increase of the model-space dimension by an order of magnitude from 2.7×10^9 to 2.5×10^{10}. More details on the technical development of our NCSM code can be found in Appendix A.

IV. s-SHELL NUCLEI: VALIDATION AND CONVERGENCE

A. $A = 3$ nuclei

The three-nucleon bound states of ^{3}H and ^{3}He can be computed virtually exactly. While there is little need for IR extrapolations of these calculations, they allow us to validate the IR extrapolation scheme and to check the relation Eq. (15) between the separation energy and the momentum k_∞. The bound-state energies of these nuclei are converged in the largest $N_{\max} = 40$ spaces we employ, and we find $E(^3\mathrm{He}) = -7.52$ MeV and $E(^3\mathrm{H}) = -8.25$ MeV. The corresponding separation energies with respect to the deuteron [$E(^2\mathrm{H}) = -2.2246$ MeV for the interaction NNLO$_{\mathrm{opt}}$] give $k_{\mathrm{sep}} \approx 0.50$ and 0.54 fm^{-1} from Eq. (14) for ^{3}He and ^{3}H, respectively.

We fix the UV cutoff Λ, and for Hilbert spaces with $N_{\max} \leqslant \max(N_{\max})$ compute the corresponding oscillator length [i.e., the oscillator spacing $\hbar\omega(N,\Lambda)$], using the tables presented in Ref. [26] for the function $f(N)$ in Eq. (5) for the nucleus ^{3}H. This yields Hilbert spaces with identical UV cutoffs and different IR lengths L. At these fixed Λ, we compute the ground-state energies $E(L,\Lambda)$ and point-proton radii $r(L,\Lambda)$ and perform IR extrapolations.

Let us discuss first the extrapolation of energies. The χ^2 fits of Eq. (2) to computational data employ the uncertainty Eq. (3). This uncertainty is a naive estimate of subleading corrections to Eq. (2) and ensures that numerical data is weighted correctly as a function of L. The results for ^{3}H energies are shown in Fig. 4. The squares show the variational minimum of the computed energy as a function of the UV cutoff and for a given $N_{\max}$. The extrapolated results are shown as circles, with uncertainty estimates given by Eq. (3), scaled with the extrapolation distance, presented as a band.

We see that the extrapolated results are a significant improvement over the NCSM results; with increasing $N_{\max}$ they stabilize and are constant over an increasing range of UV cutoffs. We note that the uncertainties only estimate higher-order IR corrections due to the first open decay channel. Missing UV corrections, or IR corrections from other decay channels (with a separation momentum $k_{\mathrm{sep}} > k_\infty$), are not included. For the triton, for instance, the separation into three nucleons has a separation momentum $k_{\mathrm{sep}}(t \to p + n + n) \approx 0.63$ fm^{-1}. This momentum is not much larger than the separation momentum for the disintegration $t \to d + n$. We

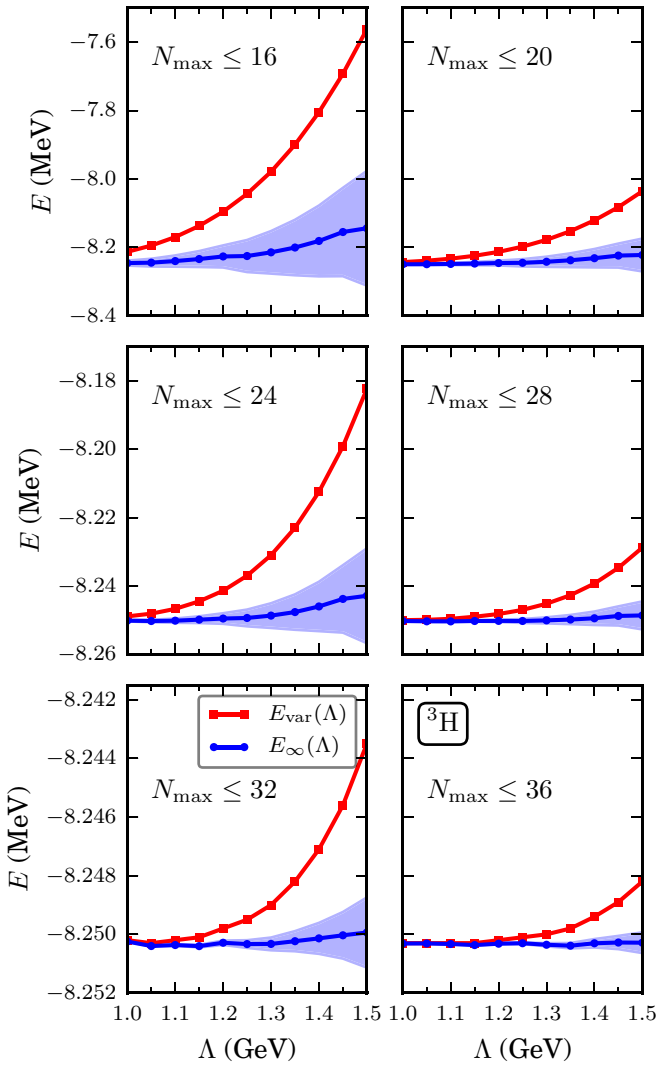

FIG. 4. Extrapolated energy $E_\infty(\Lambda)$ (circles) for ^{3}H with the NNLO$_{\rm opt}$ *NN* interaction. The different panels correspond to different NCSM model space truncations from $\max(N_{\max}) = 16$ to $\max(N_{\max}) = 36$. The bands estimate uncertainties from subleading IR corrections. The squares denote the minimum energy computed with the NCSM as a function of Λ.

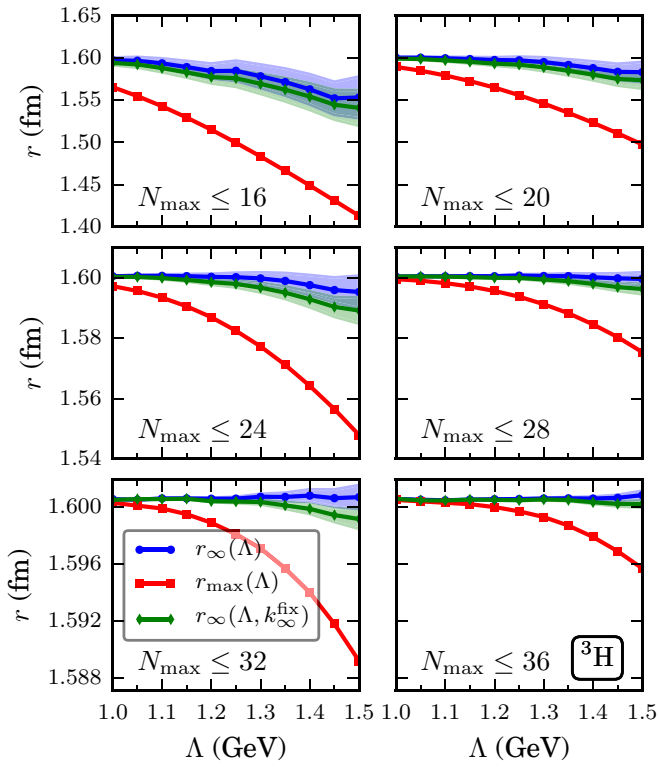

FIG. 5. Extrapolated ground-state (point-proton) radii $r_\infty(\Lambda)$ (circles) for ^{3}H with the NNLO$_{\rm opt}$ *NN* interaction. The different panels correspond to different NCSM model space truncations from $\max(N_{\max}) = 16$ to $\max(N_{\max}) = 36$. The bands estimate uncertainties from subleading IR corrections. The squares denote the maximum radius computed with the NCSM as a function of Λ and model space truncation.

note that the displayed uncertainties increase with increasing Λ, because at fixed $N_{\max}$ the IR length L decreases with increasing Λ.

The results for the extrapolated point-proton radius are presented in Fig. 5 as circles and compared to the values obtained from the NCSM calculations. Here, diamonds show extrapolation results when k_∞ is fixed from the energy extrapolation. These resulted in the reproduction of the exact ground-state energies in the interval 1000 MeV $\lesssim \Lambda \lesssim$ 1300 MeV. In general, the extrapolation that leaves k_∞ as an adjustable parameter (circles) yields more stable extrapolated radii, and the extrapolated radius can be read off the plateau that develops as $N_{\max}$ is increased. In the χ^2 fits of the radius, we use the uncertainty Eq. (7) to account for subleading corrections. These uncertainties, scaled with the extrapolation distance, are also shown as bands in Fig. 5.

The values for k_∞ resulting from the fit of Eq. (2) are shown in Fig. 6(b). We find that a stable region is reached for large enough UV scales. We note that fits performed at a UV cutoff Λ below the variational minimum have UV corrections that are larger than the IR corrections. This is reflected in a Λ dependence of the fit parameters a_0 and k_∞. The values for k_∞ obtained from the radius extrapolation are shown in Fig. 6(c). In large model spaces, the values obtained from the fit of energies and radii agree with each other. We present the average value of these two fit parameters, $k_\infty = 0.54(1)$ (obtained at the largest $N_{\max}$ and Λ), as the recommended result in Table I. This numerical result validates our derivation in Sec. II since the momentum scale extracted from the fits agrees very well with the separation momentum $k_{\rm sep}(^3{\rm H}) \approx 0.54\,{\rm fm}^{-1}$ obtained from the computed binding energies with the NNLO$_{\rm opt}$ interaction.

Values of a_0 from the fit to Eq. (2) are shown in Fig. 6(a). For the largest $N_{\max}$ and Λ we find $a_0 \approx 280$ MeV, which corresponds to the ANC $\gamma_{\rm sep} \approx 3.5\ {\rm fm}^{-1/2}$ in the orthogonal Jacobi coordinate ρ_1. Using the results of Appendix C, the ANC in the physical separation coordinate then becomes $(2/3)^{1/4}\gamma_{\rm sep} \approx 3.2\ {\rm fm}^{-1/2}$. We compare this value with the experimental data of Refs. [42,43], noting that experiments provide us with a dimensionless normalization parameter. We use Eq. (19) in the review [42] to convert this to an ANC

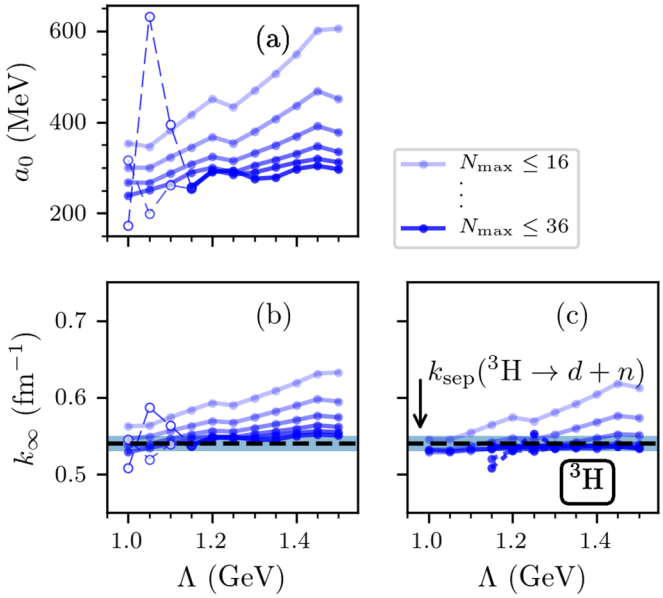

FIG. 6. Fit parameters a_0 (a), $k_\infty(\Lambda)$ for ^{3}H energy extrapolation (b), and $k_\infty(\Lambda)$ for radius extrapolation (c) for different NCSM model space truncations from $\max(N_{\max}) = 16$ to $\max(N_{\max}) = 36$. Open symbols denote results for which UV corrections are expected to be larger than IR ones, and the corresponding fits are unreliable. The lowest, theoretical separation momentum is given as a dashed line with an uncertainty band.

of $2.1 - 3.4$ fm$^{-1/2}$, in agreement with our theoretical value extracted from the fit.

These numerical results suggest that the relevant low-momentum scale for a bound state in a many-body system indeed is set by the momentum corresponding to the smallest separation energy. We note that this conclusion is not limited to the oscillator basis, as similar results were found for the lattice [29]. Of course, this is consistent with view on the ANC, which governs astrophysical reaction rates [32] at lowest energies.

We use the extrapolations at fixed $\Lambda = 1200$ MeV to extract a sequence of recommended values for the ground-state energy and the point-proton radius for ^{3}H as a function of the model-space truncation; see Fig. 7. For ^{3}He we find results of similar quality; they are given in Appendix B.

Below, we will see that Eq. (15) is also semiquantitatively fulfilled in $A = 4$,6 and 16-body systems.

TABLE I. Recommended results for the ground-state energy E_∞ (in MeV) and point-proton radius r_∞ (in fm) for different nuclei. All results are obtained with the NNLO$_{\rm opt}$ NN interaction. The variational minimum $E_{\rm var}^{\rm min}$ for each nucleus computed at the largest $N_{\max}$ reached in the NCSM calculations is also shown. Finally, the momentum scale, k_∞ (extracted from the energy and radius fits), is compared with the lowest separation momentum, $k_{\rm sep}$, for this interaction from Eq. (14).

	E_∞	r_∞	$E_{\rm var}^{\rm min}$	$N_{\max}$	k_∞	$k_{\rm sep}$
^{3}H	−8.250	1.60	−8.250	40	0.54(1)	0.54(1)
^{3}He	−7.502	1.793	−7.502	40	0.51(2)	0.51(1)
^{4}He	−27.592	1.434	−27.592	20	0.84(5)	0.97(3)
^{6}Li	−30.59(3)	2.42(2)	−30.500	22	0.44(5)	0.19(8)
^{6}He	−27.3(2)	1.84(2)	−26.976	16	0.47(3)	–
^{8}He	−26.5(1.1)	1.82(3)	−24.631	12	0.42(3)	–

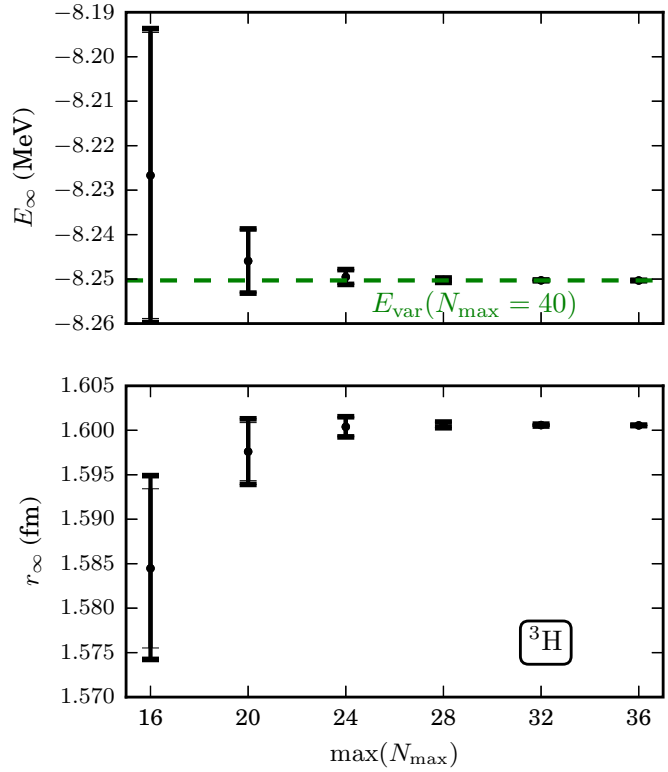

FIG. 7. Recommended results for the ^{3}H energy (upper panel) and radius (lower panel) for different NCSM model space truncations from $\max(N_{\max}) = 16$ to $\max(N_{\max}) = 36$.

B. ^{4}He

In this Section we present the IR extrapolations for the ground-state energy and point-proton radius of ^{4}He. The top panel of Fig. 8 shows the ground-state energies for ^{4}He in model spaces with $N_{\max} = 4,6,\ldots,20$ as a function of the oscillator spacing $\hbar\omega$. Solid lines connect data points with equal $N_{\max}$. Dashed lines connect data points with equal Λ, starting at $\Lambda = 750$ MeV to $\Lambda = 1500$ MeV (from left to right in steps of 50 MeV). In what follows, we will perform IR extrapolations with Eq. (2) based on data points computed in model spaces with equal UV cutoff Λ.

The lower panel of Fig. 8 shows the computed ground-state point-proton radius for ^{4}He as a function of the oscillator spacing for model spaces of size $N_{\max}$ as indicated. Solid lines again connect radii at fixed $N_{\max}$ while dashed lines connect data at fixed UV cutoff Λ. The results become almost independent of $N_{\max}$ around $\hbar\omega \approx 23$ MeV, and it makes sense to identify this value as the theoretical radius in an infinite space; see, e.g., Refs. [17,41,44]. Below we will see that the radius extrapolations yield plateaus that allow one to read off the radius with more confidence also when no full convergence can be achieved.

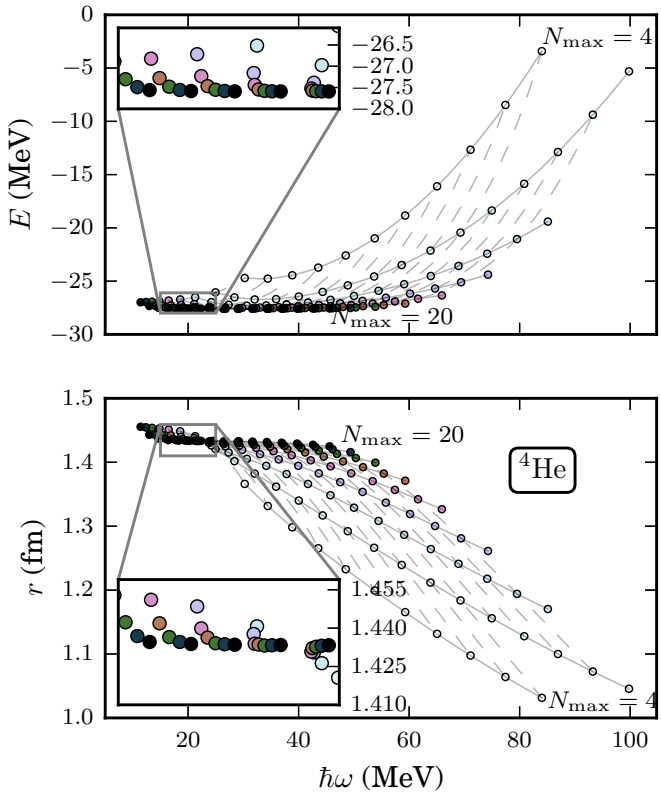

FIG. 8. Computed ground-state energies (upper panel) and point-proton radii (lower panel) for ^{4}He as a function of the oscillator spacing $\hbar\omega$ in model spaces of size $N_{\max}$ as indicated. Solid lines connect data points with equal $N_{\max}$. Dashed lines connect data points with equal UV cutoff Λ, starting at $\Lambda = 750$ MeV to $\Lambda = 1450$ MeV (from left to right in steps of 50 MeV).

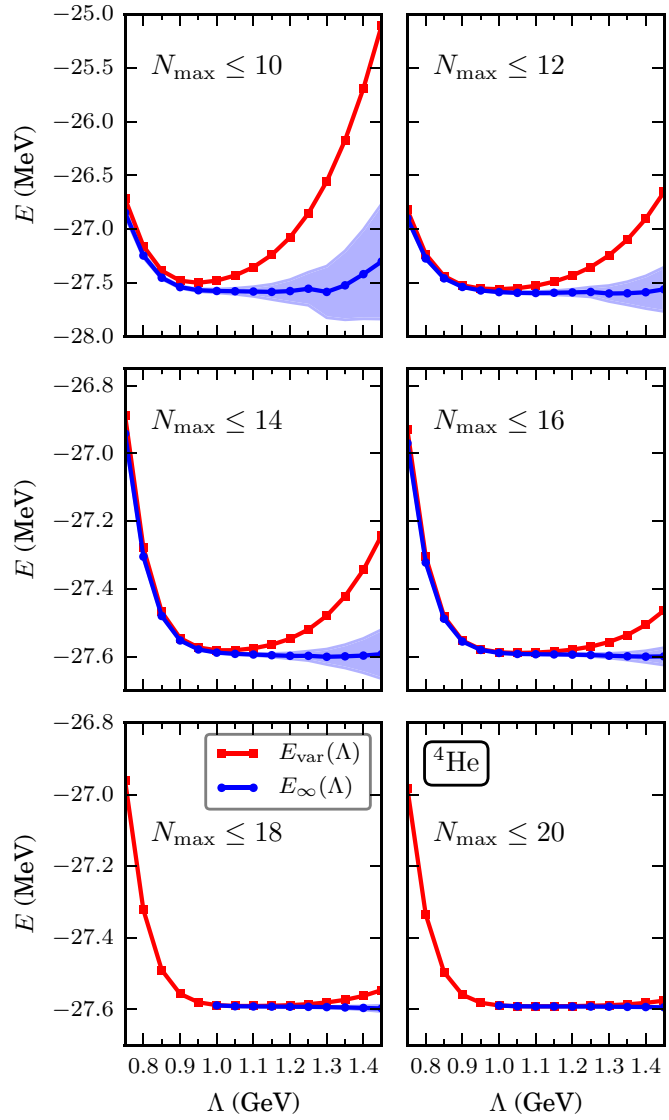

FIG. 9. Extrapolated energy $E_\infty(\Lambda)$ (circles) for ^{4}He. The different panels correspond to different NCSM model space truncations from $\max(N_{\max}) = 10$ to $\max(N_{\max}) = 20$. See caption of Fig. 4 for further details.

The trend of the radius curves can be understood as follows. With increasing oscillator spacings, the computed radius decreases because the IR length of the model space also decreases. In this regime, UV corrections to the bound-state become increasingly smaller. For decreasing values of the oscillator spacing, the UV cutoff Λ decreases, and the computed binding energy decreases, thus leading to a more weakly bound system and an ever increasing radius. In this regime, IR corrections to the radius become increasingly smaller as the oscillator spacing is further decreased.

We perform a χ^2 fit to the ground-state energies $E(L,\Lambda)$ based on the extrapolation Eq. (2) and use the theoretical uncertainties Eq. (3) in the fit. We recall that this uncertainty only accounts for some of the missing IR corrections. Missing UV corrections are not addressed and one should therefore not expect a proper error estimate for small values of Λ. The fit results for the parameters $E_\infty(\Lambda)$ are shown as circles in Fig. 9 for various values of $N_{\max}$. We see that the extrapolation energies are an improvement compared to the variational minima (shown as squares).

For the ground-state radius we perform χ^2 fits of Eq. (6) to our computed results, using the uncertainty Eq. (7) to account for subleading corrections. The results for r_∞ and the corresponding uncertainty estimates are shown as circles and bands in Fig. 10; here we used k_∞ as a fit parameter. In contrast, one might also employ for k_∞ the same values as found in the energy extrapolation. Employing the latter in the fit of the radii [i.e., making only r_∞ and α adjustable parameters in Eq. (6)] yields extrapolated results that are shown as diamonds in Fig. 10, with a green uncertainty band. In very large spaces, both extrapolation results approach each other. In smaller spaces, extrapolated radii exhibit a weaker Λ dependence if k_∞ is an adjustable parameter. The extrapolation results can be compared to the computed NCSM results (squares).

The results for the fit parameter k_∞ from the energy and radius extrapolations are shown in the top and bottom panels of Fig. 11, respectively. For the largest model spaces and cutoffs around 1 GeV they are consistent with (but not identical to) each other. The $N_{\max}$ dependence of k_∞ is smallest for the energy extrapolation, and we focus on

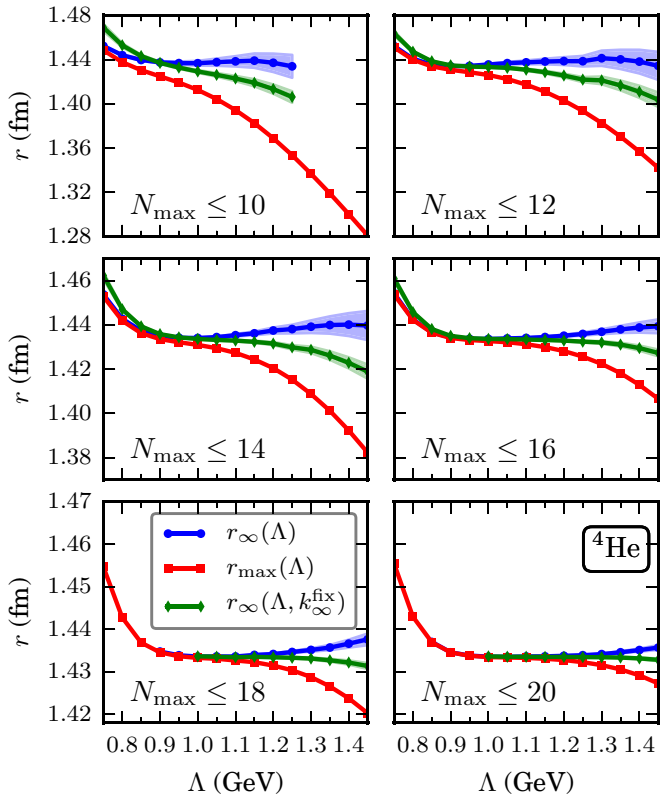

FIG. 10. Extrapolated ground-state (point-proton) radii $r_\infty(\Lambda)$ (circles) for ^{4}He. The different panels correspond to different NCSM model space truncations from $\max(N_{\max}) = 10$ to $\max(N_{\max}) = 20$. See caption of Fig. 5 for further details.

them. We note that k_∞ depends weakly on Λ as this quantity increases beyond $\Lambda \gtrsim 1000$ MeV. This is consistent with our expectations because these results are increasingly well UV converged. We find $k_\infty \approx 0.87 \pm 0.03$ fm^{-1} from the energy extrapolation and compute a corresponding separation energy

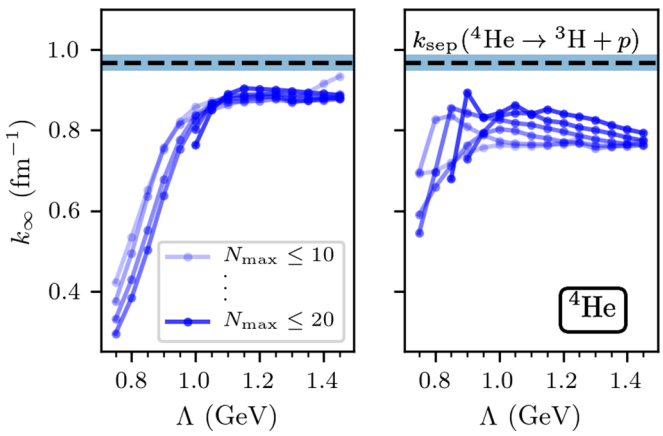

FIG. 11. Fit parameter $k_\infty(\Lambda)$ for ^{4}He energy extrapolation (left panel) and radius extrapolation (right panel) for different NCSM model space truncations from $\max(N_{\max}) = 10$ to $\max(N_{\max}) = 20$. The lowest, theoretical separation momentum is given as a dashed line with an uncertainty band.

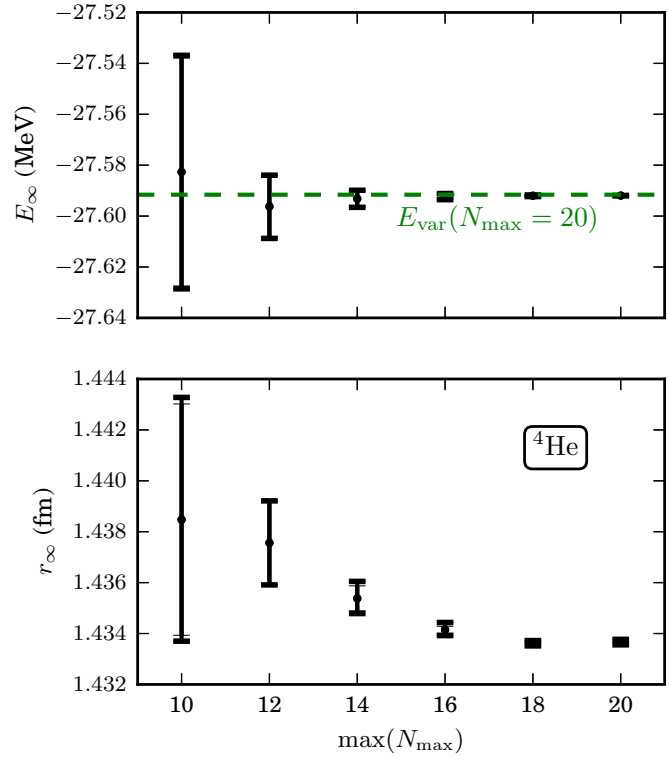

FIG. 12. Recommended results for the ^{4}He energy (upper panel) and radius (lower panel) for different NCSM model space truncations from $\max(N_{\max}) = 10$ to $\max(N_{\max}) = 20$.

$S = \frac{k_\infty^2}{2m} \approx 15.8 \pm 1.1$ MeV. This value is somewhat smaller than the theoretical values for the proton and neutron separation energies $S_p \approx 19.3$ MeV and $S_n \approx 20.1$ MeV, respectively. The corresponding separation momenta are $k_{\rm sep} \approx 0.96$ and 0.98 fm^{-1}, see Table I, about 10% larger than from our energy extrapolation.

We note that the two-nucleon separation energies are significantly larger than the nucleon separation energy of about 20 MeV. Thus, they should yield only smaller and negligible corrections. Furthermore, the ^{4}He nucleus is essentially an s-wave state, and corrections to the energy extrapolation Eq. (1) due to other partial waves are also expected to be small.

We collect recommended values for ground-state energy and the charge radius of ^{4}He in the panels of Fig. 12. The extrapolated values and corresponding uncertainties are taken at $\Lambda = 1100$ MeV.

V. *p*-SHELL NUCLEI: LOW-MOMENTUM SCALES OF MANY-BODY SYSTEMS

A. ^{6}Li

^{6}Li is a weakly bound nucleus due to the proximity of the $^6{\rm Li} \to {}^4{\rm He} + d$ breakup channel at only 1.5 MeV excitation energy. The experimental charge radii $r_c(^A{\rm Li}) = 2.5432(262)$, 2.4173(28), and 2.327(30) fm for $A = 6$, 7, and 8, respectively [45], confirm that ^{6}Li can be viewed as a deuteron-halo nucleus. This makes *ab initio* computation of this nucleus somewhat challenging [41,46,47], and IR extrapolations can be useful.

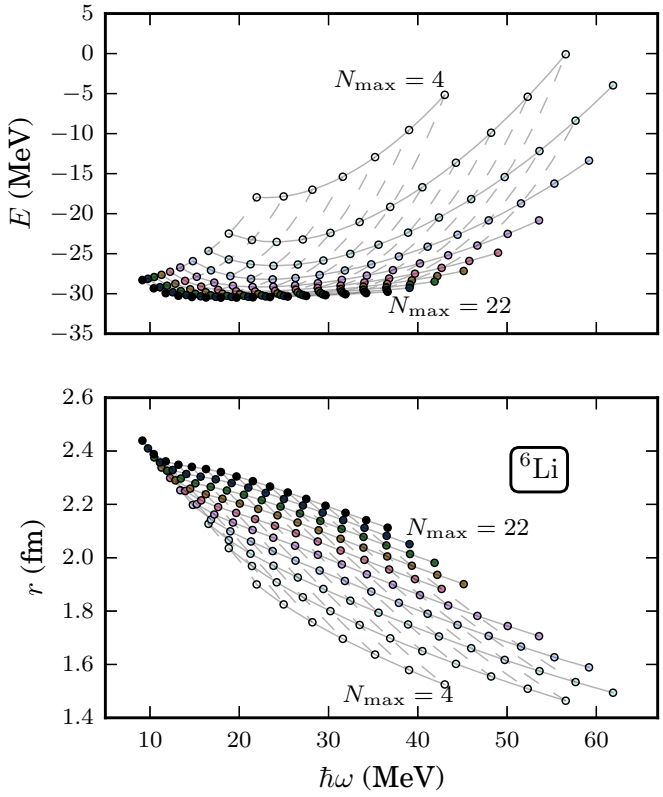

FIG. 13. Computed ground-state energies (upper panel) and point-proton radii (lower panel) for ^{6}Li as a function of the oscillator spacing $\hbar\omega$ in model spaces of size $N_{\max}$ as indicated. Solid lines connect data points with equal $N_{\max}$. Dashed lines connect data points with equal UV cutoff Λ, starting at $\Lambda = 750$ MeV to $\Lambda = 1400$ MeV (from left to right in steps of 50 MeV).

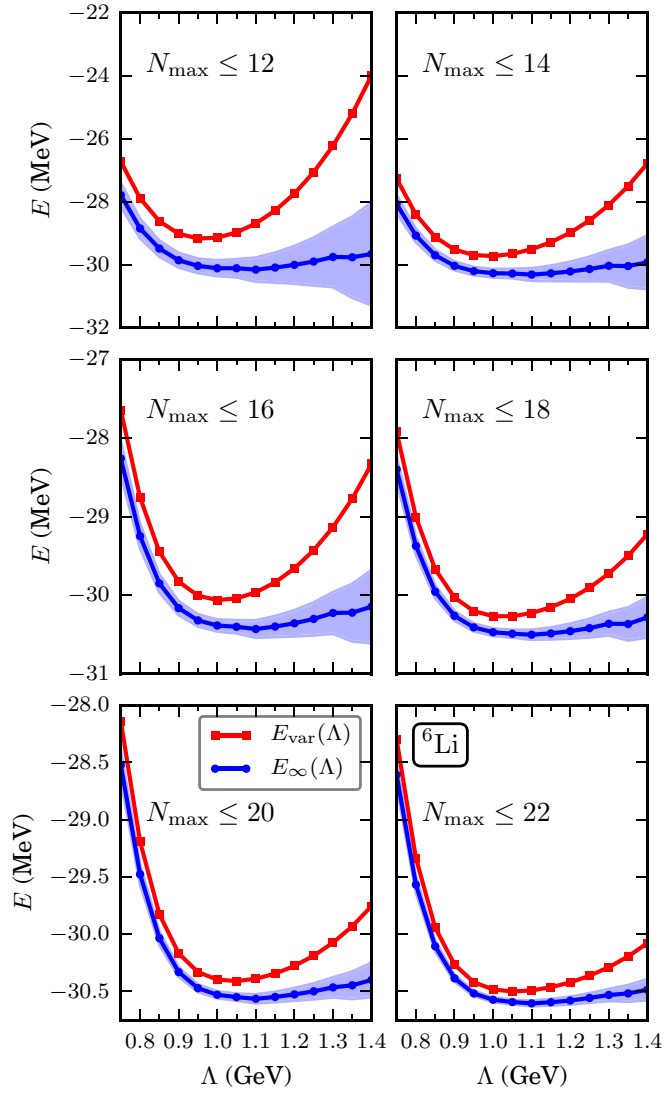

FIG. 14. Extrapolated energy $E_\infty(\Lambda)$ (circles) for ^{6}Li. The different panels correspond to different NCSM model space truncations from $\max(N_{\max}) = 12$ to $\max(N_{\max}) = 22$. See caption of Fig. 4 for further details.

At fixed UV cutoff Λ and N we compute the corresponding oscillator spacing $\hbar\omega(N,\Lambda)$, using the tables presented in Ref. [26] for the nucleus ^{6}Li. We choose model spaces with $N \leqslant N_{\max}$ and compute the ground-state energy and its point-proton radius. The upper panel of Fig. 13 shows the ground-state energies for ^{6}Li in model spaces with $N_{\max} =$ 4,6,8 . . . ,22 as a function of the oscillator spacing $\hbar\omega$.

For the radii in the lower panel, many lines merge around $r \approx 2.3$ fm at $\hbar\omega \approx 12$ MeV, and one might be tempted to identify this almost-$N_{\max}$-independent value as the theoretical radius in an infinite space. As we will see below, however, IR extrapolations yield a larger radius than this merging point might suggest.

We perform a χ^2 fit to the resulting energies based on the extrapolation Eq. (2) and use the theoretical uncertainties Eq. (3). The fit results for the energy $E_\infty(\Lambda)$ are shown in Fig. 14. We see that for a range of Λ around 1100 MeV, the IR extrapolation significantly improves over the variational minimum. For smaller values of $\Lambda \lesssim 1000$ MeV (but still above the UV cutoff of NNLO$_{\rm opt}$ $\Lambda_\chi = 500$ MeV), the lack of UV convergence yields energies that increase with decreasing values of Λ. For larger values of $\Lambda \gtrsim 1200$ MeV the extrapolated energies increase as Λ is increased. This can be understood as follows: At large values of Λ, UV convergence is presumably achieved. However, as is reflected by the increasing theoretical uncertainties, the maximum L values achievable in spaces with $N \leqslant N_{\max}$ decrease with increasing Λ, and we are not any more in the regime where the asymptotic Eq. (2) is valid. We recall that at smaller values of L subleading IR corrections to Eq. (2) must become relevant, leading to a more complicated nonexponential (i.e., slower than exponential) IR convergence. Fitting such data points with an exponential yields higher values for E_∞. These results at high values of Λ are consistent with Refs. [26,30] where IR extrapolations for fully UV-converged ground-state energies are close to the variational minimum, thus questioning the utility of such extrapolations.

Our results for the point-proton radius are shown in Fig. 15 for increasing values of $N_{\max}$. The raw results $r(N_{\max},\Lambda)$ are shown as red squares. Blue circles show extrapolated results where k_∞ is treated as a fit parameter; here,

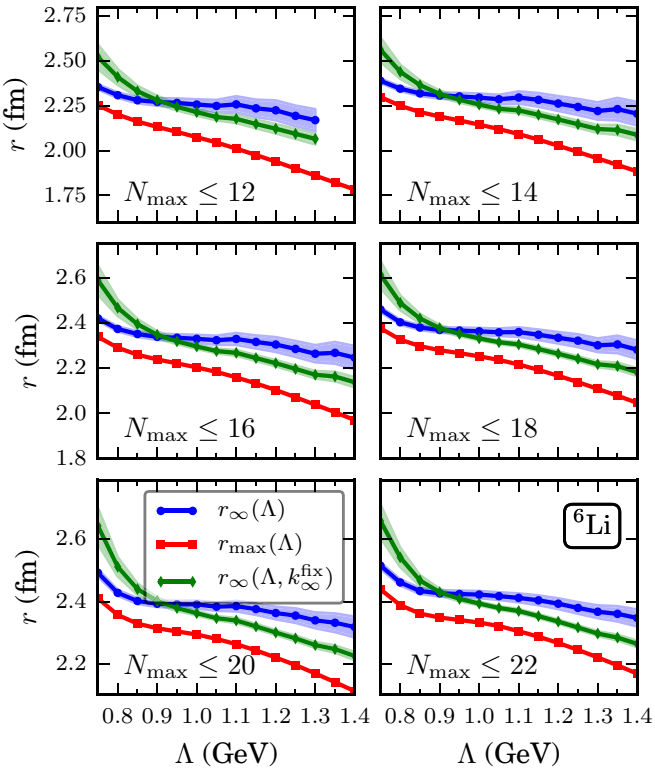

FIG. 15. Extrapolated ground-state (point-proton) radii $r_\infty(\Lambda)$ (circles) for ^{6}Li. The different panels correspond to different NCSM model space truncations from $\max(N_{\max}) = 12$ to $\max(N_{\max}) = 22$. See caption of Fig. 5 for further details.

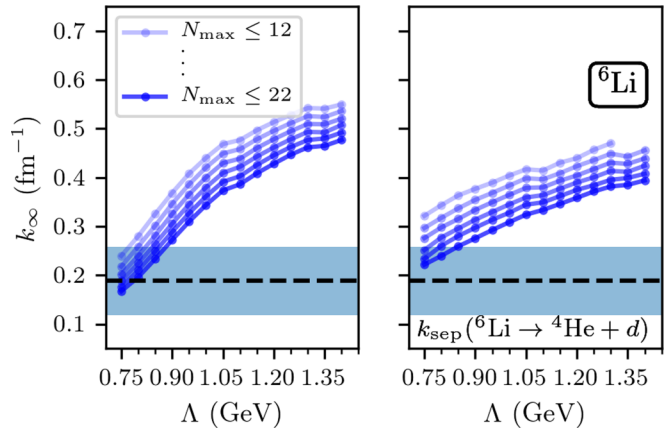

FIG. 16. Fit parameter $k_\infty(\Lambda)$ for ^{6}Li energy extrapolation (left panel) and radius extrapolation (right panel) for different NCSM model space truncations from $\max(N_{\max}) = 12$ to $\max(N_{\max}) = 22$. The lowest, theoretical separation momentum is given as a dashed line with an uncertainty band.

Λ-independent plateaus develop as $N_{\max}$ is increased. Green diamonds show extrapolation results where k_∞ is taken from the energy extrapolation; while the results display a weaker Λ dependence than the raw data, no plateaus are formed in this case. Our extrapolated radius result, $r_\infty = 2.417 \pm 0.02$ fm, yields a charge radius $r_c = 2.55(2)$ fm in agreement with data [45], and the theoretical uncertainty also reflects that our radius is not yet fully converged. Here we used the well-known formula $r_c^2 = r_\infty^2 + \langle r_p^2 \rangle + (N/Z)\langle r_n^2 \rangle + 0.033$ fm^2, where $\langle r_p^2 \rangle = 0.769$ fm^2 and $\langle r_n^2 \rangle = -0.116$ fm^2 are the mean-squared charge radii of the proton and neutron, respectively, and the last correction is the Darwin-Foldy term.

The momenta k_∞ resulting from the energy and radius extrapolation are shown in the left and right panel of Fig. 16, respectively. These momentum parameters only start to stabilize for the largest values of Λ, perhaps suggesting that UV convergence is about to be reached. We note that k_∞ still decreases by about 0.02 fm^{-1} as $N_{\max}$ is increased from 14 to 16 (and from 16 to 18). The values from the energy and radius extrapolation both lack IR convergence and differ by about 20%.

For ^{6}Li, the deuteron separation energy (or the α-particle separation energy) is $S_\alpha \approx 1.6$ MeV experimentally and about 0.8 MeV when computed from the binding energy difference between ^{6}Li on the one hand, and ^{4}He and ^{2}H on the other hand. This small separation energy makes the computation of the binding energy and radius of this nucleus a challenge in *ab initio* calculations. Single-nucleon separation energies are significantly larger, and corresponding IR corrections are thus much smaller. At $\Lambda_{\text{UV}} = 1500$ MeV in the largest model spaces, we have $k_\infty L \approx 4$, barely in the regime $k_\infty L \gg 1$ that is required for IR extrapolations. As the ^{6}Li nucleus has significant s-wave and p-wave contributions, the corresponding $(k_\infty L)^{-1}$ corrections to the IR extrapolation formula Eq. (1) could still be sizable. This is possibly also reflected in the slow convergence of k_∞. Taking a value of $k_\infty \approx 0.44 \pm 0.05$ fm^{-1} from the extrapolations we find for the separation energy,

$$S_\alpha = \frac{\hbar^2 k_\infty^2}{2m} \approx 3.9 \pm 1\,\text{MeV}. \tag{18}$$

This is still larger than expected from binding-energy differences. We note that our value for k_∞ is consistent with the value $k_\infty \approx 0.49$ fm^{-1} reported in Ref. [26].

Recommended values for the ground-state energy of ^{6}Li are shown in the top panel of Fig. 17.

B. ^{6,8}He

We also computed the nuclei ^{6,8}He. In finite model spaces, the binding energies of these nuclei are smaller than the binding energy of ^{4}He. Thus, they are unbound with respect to emission of the alpha-particle. While this is a shortcoming of the employed NNLO$_{\text{opt}}$ interaction, it is still interesting to study these cases in more detail. In an infinite space, the ^{6,8}He systems are thus a ^{4}He nucleus and free neutrons, and the expectation is that the ground-state energy is that of the ^{4}He nucleus (as kinetic energies of the neutrons can be arbitrarily small and the s-wave scattering of neutrons among each other and off the ^{4}He nucleus yields arbitrary small contributions). Thus, the wave functions of the ^{6,8}He systems would not fall off exponentially, and the extrapolation formulas could not be applied. However, when applying the extrapolation formulas to these systems, we still got meaningful results, i.e., the energy

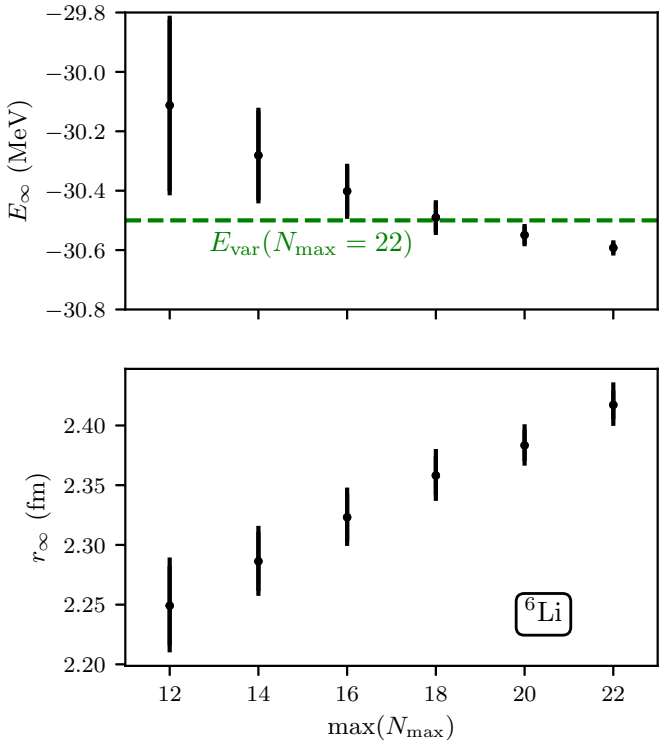

FIG. 17. Recommended results for the ^{6}Li energy (upper panel) and radius (lower panel) for different NCSM model space truncations from $\max(N_{\max}) = 12$ to $\max(N_{\max}) = 22$.

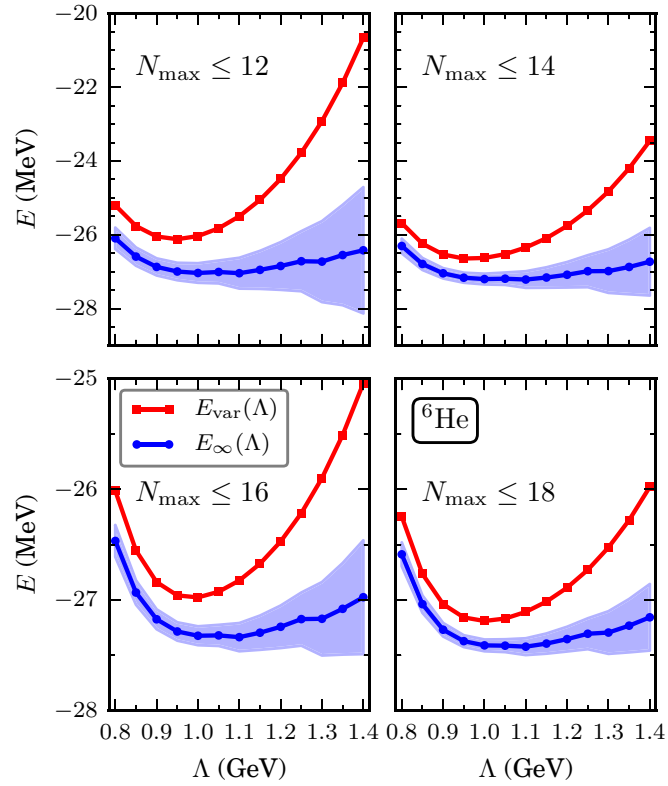

FIG. 18. Extrapolated ground-state energy $E_\infty(\Lambda)$ for ^{6}He. The different panels correspond to different NCSM model space truncations. See caption of Fig. 4 for further details.

seems to converge exponentially with increasing size L of the model space. This unexpected result is shown in Fig. 18 for ^{6}He.

How can this be understood? The model spaces we employ have a maximum extent (i.e. a corresponding hard-wall radius) of about $L \approx 10$ fm in position space. The ^{6,8}He nuclei have nucleons with angular momentum $l = 1$ in a simple shell-model picture, and grand angular momentum $K = 2$ in hyperspherical coordinates. The corresponding angular momentum barrier is $\hbar^2(K + 3/2)(K + 5/2)/(2mL^2) \approx 3$ MeV high even at the hard-wall radius. (For ^{4}He we have $K = 0$ and the barrier is less than an MeV at the boundary.) Thus, the binding of the ^{6}He nucleus is a transient behavior that appears in model spaces that are sufficiently large to exhibit a convergence of results but still too small to reflect the asymptotic true nature of this six-nucleon system.

The top panel of Fig. 19 shows the corresponding k_∞ values obtained from the extrapolation of the ground state energy. These values are still not converged.

We also performed coupled-cluster computations [10,48] of ^{8}He in the Lambda-CCSD(T) approximation [49]. These calculations employ a model space that is a product of single-particle spaces. We denote the truncation of this space with $N_{\rm sp,max}$. The relevant IR lengths [and UV cutoffs via Eqs. (5)] are taken from Ref. [25]. The results for the ground-state energy are shown in Fig. 20, using the same energy scale as for the NCSM results. We note that both methods yield an extrapolated ground-state energy for ^{8}He somewhat below -26 MeV. However, the employed model spaces and UV cutoffs Λ differ from each other.

For the product space employed in the coupled-cluster computations, we have not been able to relate the fit parameter k_∞ to an observable. We note that the result for k_∞ in NCSM and coupled-cluster calculations differ from each other.

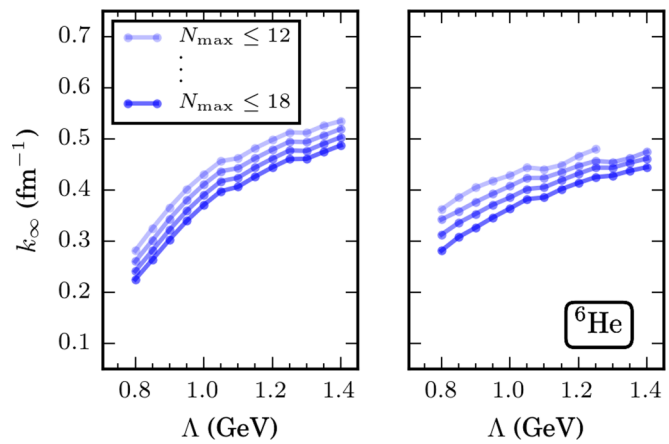

FIG. 19. Fit parameter $k_\infty(\Lambda)$ for ^{6}He energy extrapolation (left panel) and radius extrapolation (right panel) for different NCSM model space truncations from $\max(N_{\max}) = 12$ to $\max(N_{\max}) = 18$.

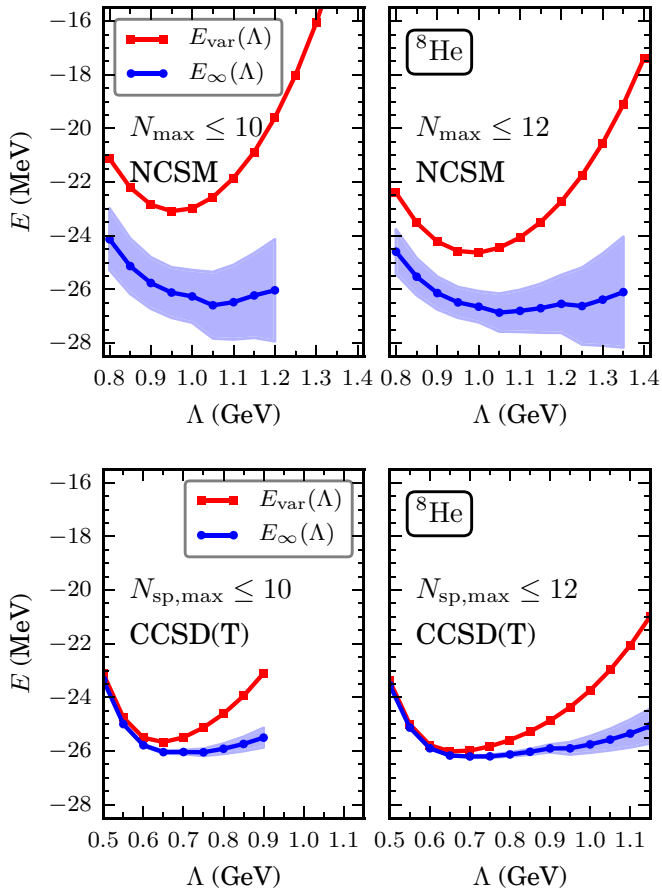

FIG. 20. Extrapolated energy $E_\infty(\Lambda)$ (circles) for ^{8}He from the NCSM (upper panels) and the coupled-cluster method (lower panels) with different model space truncations. The band estimates uncertainties from subleading IR corrections. The squares denote the minimum energy computed with the respective method as a function of Λ.

C. ^{16}O

Wendt *et al.* [26] reported NCSM results for ^{16}O using the *NN* potential NNLO$_{\rm opt}$. These are expensive computations and we do not repeat them here. In their IR extrapolation, they found a fit parameter of $k_\infty \approx 0.47$ fm^{-1}. This corresponds to a separation energy of about $S \approx 4.6$ MeV. In ^{16}O, the least energetic disintegration threshold is α-particle emission, and the threshold is at 7.16 MeV experimentally. The coupled-cluster computations of ^{16}O require less effort than the NCSM and converge rapidly in the model spaces considered in this work. The results for the parameters $E_\infty(\Lambda)$ from the χ^2 fits are shown in Fig. 21.

The extrapolated energy is consistent with the (practically fully converged) value of $E \approx -130.1$ MeV obtained in model spaces with $N_{\rm sp,max} = 12$. We note that the fit of the momentum stabilizes around $k_\infty \approx 0.97$ fm^{-1}, but we have not been able to relate this value to an observable. We also note that coupled-cluster calculations in the employed Lambda-CCSD(T) approximation [49] would be insensitive to the emission of α particles as this would require at least four-particle–four-hole excitations. For the employed interaction, the neutron separation energy is about 20 MeV [35].

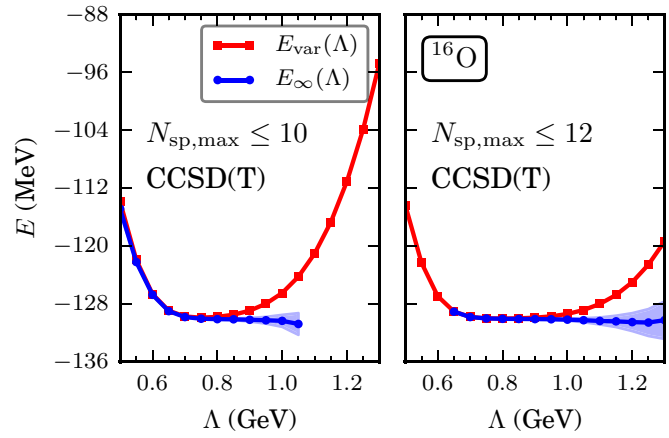

FIG. 21. Extrapolated energy $E_\infty(\Lambda)$ (circles) for ^{16}O. The different panels correspond to different model space truncations. The bands estimate uncertainties from subleading IR corrections. The squares denote the minimum energy computed with the Lambda-CCSD(T) as a function of Λ.

VI. SUMMARY AND DISCUSSION

In this paper, we presented three main results. First, we further advanced the shell-model code pANTOINE, a parallel version of the Strasbourg shell-model code ANTOINE, to deal with unprecedented large harmonic oscillator model spaces. This allowed us to present benchmark results for a variety of light nuclei and to further explore asymptotic IR extrapolation formulas. The inclusion of three-nucleon forces into this computational algorithm is an ongoing task. Second, we performed IR extrapolations of ground-state energies and radii of *p*-shell nuclei at fixed UV cutoffs in a considerable range of such cutoffs. This allowed us to improve over previous extrapolations (taken at very large UV cutoffs) and to present extrapolations with increased accuracy and precision. In particular, the extrapolated energies and radii are stable in a range of UV cutoffs and—for the ground-state energy—consistently improve over the variational minimum obtained with the available computational resources. We also found that the momentum k_∞ relevant for the extrapolation is—within our uncertainties—the same for ground-state energies and radii. Third, the extrapolation results support the hypothesis that the momentum k_∞ (which is the smallest relevant momentum for ground-state energies and radii) corresponds to the momentum of the lowest-energetic separation channel. This identification could be interesting for EFT arguments in general and for uncertainty quantification in particular. We recall that it is not really established what is the typical or relevant momentum scale in finite nuclei. Estimates range from the inverse of the nucleon-nucleon scattering length on the small side to the Fermi momentum on the high side. Our results suggest that k_∞ is the smallest relevant scale. This could imply that the precise reproduction of nucleon-nucleon scattering data at momenta below k_∞ is probably not necessary for the computation of well-bound nuclear states. Of course, (excited) states closer to threshold could require more accurate properties of the nucleon-nucleon interaction at lowest momenta.

ACKNOWLEDGMENTS

We thank Dean Lee for useful discussions. G.H. and T.P. gratefully acknowledge the hospitality of the Department of Physics at Chalmers during the initial phase of this project. The visit was supported by the Swedish Foundation for International Cooperation in Research and Higher Education (STINT, Grant No. IG2012-5158). This work was also supported by the US Department of Energy, Office of Science, Office of Nuclear Physics under Awards No. DEFG02-96ER40963 (University of Tennessee), No. DE-SC0008499, and No. DE-SC0018223 (SciDAC NUCLEI Collaboration), the Field Work Proposal ERKBP57 at Oak Ridge National Laboratory (ORNL), and under Contract No. DE-AC05-00OR22725 (Oak Ridge National Laboratory). Some of the computations were performed on resources provided by the Swedish National Infrastructure for Computing (SNIC) at C3SE (Chalmers) and NSC (Linköping).

This manuscript has been coauthored by UT-Battelle, LLC under Contract No. DE-AC05-00OR22725 with the US Department of Energy. The United States Government retains and the publisher, by accepting the article for publication, acknowledges that the United States Government retains a nonexclusive, paid-up, irrevocable, world-wide license to publish or reproduce the published form of this manuscript, or allow others to do so, for United States Government purposes. The Department of Energy will provide public access to these results of federally sponsored research in accordance with the DOE Public Access Plan (http://energy.gov/downloads/doe-public-access-plan).

APPENDIX A: TECHNICAL DETAILS OF THE pANTOINE NCSM IMPLEMENTATION

The pANTOINE NCSM code uses an iterative scheme to find the extreme eigenvalues of very large, but relatively sparse, Hermitian matrices. Matrix-vector operations consume the most execution time. Matrix-element indices are computed on-the-fly, as described in Sec. III. The code runs very efficiently on single shared-memory machines, although it requires large memory resources ($\gtrsim$32 GB). To handle vectors much larger than available memory, the operation $y = Mx$ can be split into subsets: $y_i = (M_{i1}x_1 + M_{i2}x_2 + \cdots)$.

For two-body nuclear interactions, the code generates the Hamiltonian matrix on the fly, which removes the need to distribute matrix elements over thousands of nodes. Accordingly, the results shown in Figs. 22 and 23 were obtained on a single compute node. The current production version requires node-local disk space for temporary storage. For job sizes exceeding available memory, it uses local scratch space efficiently, doing sustained multi-100 MB/s streaming reads while maintaining close to full multicore matrix-vector CPU load.

Still, the most extreme calculations for ^{6}Li require almost 10 TB of storage for Hamiltonian matrix data and Lanczos vectors (about half each); see Fig. 22(a). Even though the loaded index triple-values and matrix data is used multiple times (due to the double loops), large read speeds, as presented in Fig. 22(b), are key for being able to diagonalize matrices with dimensions surpassing 10^{10}. For $N_{\max} \geqslant 18$ the Lanczos vector is split in several blocks. With a split vector, mirror

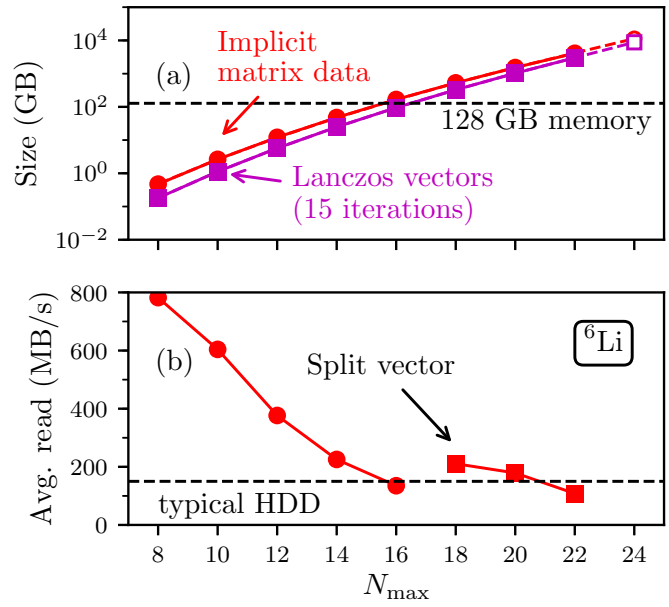

FIG. 22. pANTOINE scaling plots for the ^{6}Li nuclear many-body problem as a function of the NCSM model space truncation $N_{\max}$. The model space dimension is shown in Fig. 2. (a) Total storage required for implicit matrix construction and for 15 iterations of Lanczos vectors; (b) average read speed of implicit matrix data from disk. For $N_{\max} \geqslant 18$ the Lanczos vector is split in several blocks.

blocks are handled separately causing multiple passes over the same implicit matrix data. Since more data is read in total, the average read speed increases.

The main improvements of pANTOINE are: (i) extending the memory management to handle 64-bit offsets and thus allowing much larger working sets and subset vectors; (ii) multithreaded inner loops of the matrix-vector operations using OpenMP; (iii) speeding up the scratch I/O by the use of raw C-style functions; (iv) asynchronous read of scratch data, making most I/O be hidden under useful CPU use (matrix-vector calculations). Essentially, improvement (i) enables us to handle the larger model-spaces, while (ii) makes it feasible to run them in reasonable (but still long) times. (iii) and (iv) are needed to make (ii) significant, as I/O-related processing and waiting times otherwise dominate.

Let us use the $N_{\max} = 22$ ^{6}Li run as a specific example. There are 5200 different $nljm$ single-particle states and the resulting $M = 1$ many-body basis has the dimension 2.50×10^{10}. The full space corresponds to ~200 GB of storage space per eigenvector using double-precision for the amplitudes. Note that the proton and neutron (three-body) sub-spaces are much smaller than the full six-body space. The sub-space dimension is 1.83×10^6. There are 4.88×10^{14} nonzero matrix elements that are applied on-the-fly from 4.1 TB of implicit matrix data. However, since the data is used in different combinations, the program actually reads 24.9 TB of data from disk per iteration. At every iteration, the full matrix-vector operation requires 5.54×10^{14} multiplications, which takes a couple of days on a single compute node. The difference between number of nonzero elements and total number of multiplications come from the use of precalculated

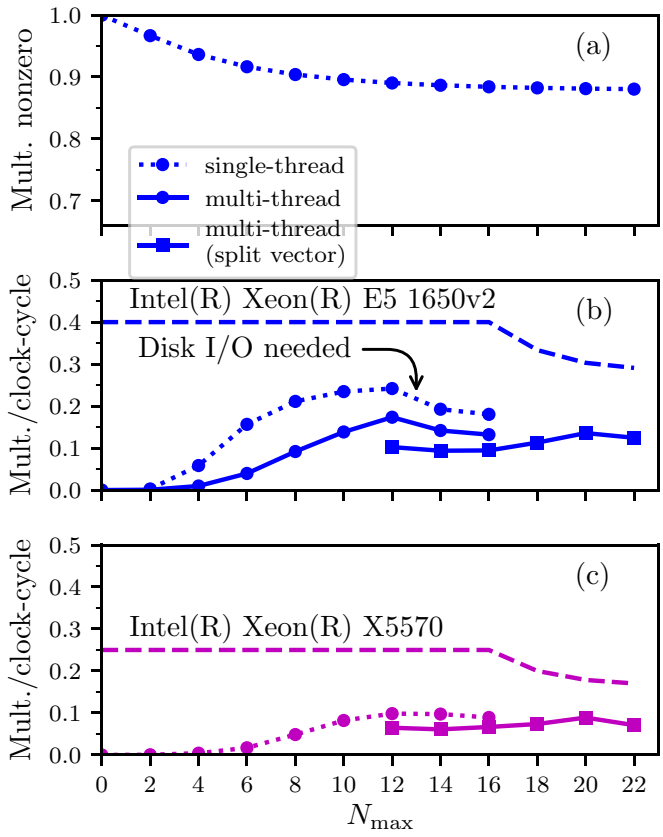

FIG. 23. pANTOINE scaling plots for the ^{6}Li nuclear many-body problem ($M = 1$) as a function of the NCSM model space truncation $N_{\max}$. (a) Multiplication efficiency (defined as the number of nonzero matrix elements divided by the actual number of multiplications being performed); multiplication per clock cycle for (b) Intel(R) Xeon(R) E5 1650v2 and (c) Intel(R) Xeon(R) X5570 using a single thread (dotted line), multiple threads (solid line with circles), and multiple-threads with splitting of the Lanczos vector (solid line with square symbols).

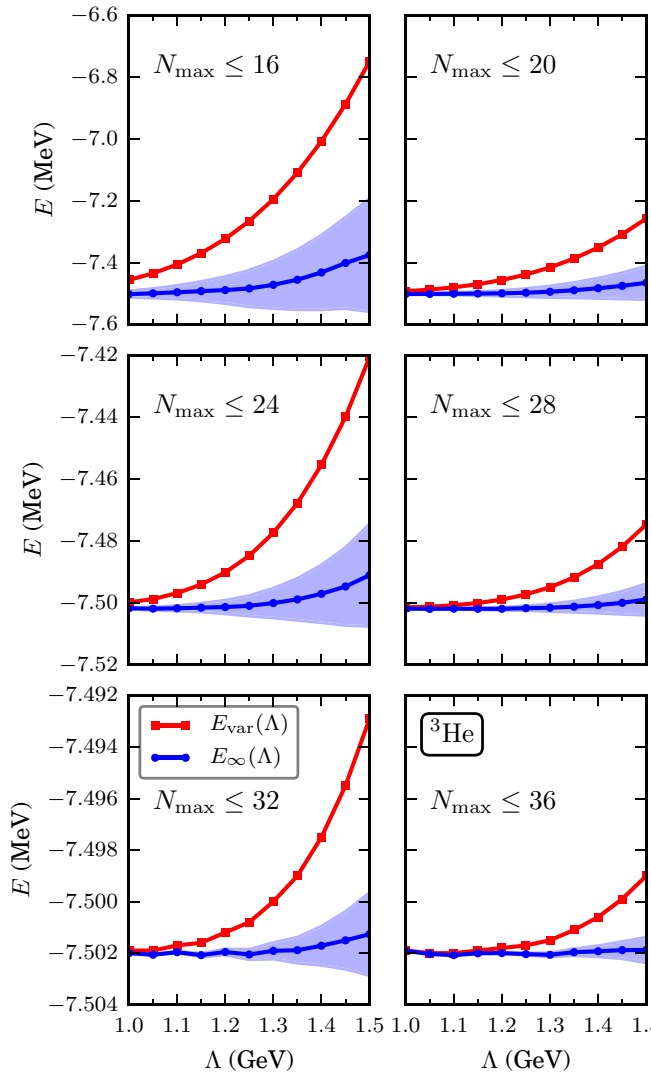

FIG. 24. Extrapolated energy $E_\infty(\Lambda)$ (circles) for ^{3}He. See caption of Fig. 4 for further details.

index-triples. It is not possible to avoid matrix-elements that vanish due to nontrivial cancellations of Clebsch-Gordan coefficients. Figure 23(a) shows how this inherent inefficiency develops with model space size.

In order for I/O reads not to act as a significant bottle-neck, a fast scratch storage component of the computer is required. Due to the multithreaded calculations needing separate large output vectors, it is also beneficial to use fewer but fast and efficient processor cores. For this calculation we used a purpose-built machine with a 6-core Xeon E5-1650v2 CPU, 128 GB of RAM and 10 × 4 TB HGST NAS disks in a RAID 5 configuration, capable of streaming scratch data at ∼1 GB/s. In this case, streaming reads averaging 108 MB/s, see Fig. 22(b), were done in parallel with maintaining a very large CPU load. The decrease in multiplication efficiency shown in Fig. 23(b) at $N_{\max} \approx 12$–14 is due to operating-system disk cache space running out, necessitating I/O each iteration. The low efficiency at the smallest $N_{\max}$ is due to block-scheduling overhead each iteration, which also is included in the measurements. The multiplication efficiencies for multi-thread runs with split vectors were measured with the Lanczos vectors divided in four roughly equal pieces, except for $N_{\max} = 22$ where sixteen pieces were used.

Despite the heavy I/O and on-the-fly computation of matrix element indices the code performed 2.40×10^9 multiplications/s in average. With 6 × 3.6 GHz available, this implies an impressive load of 0.111 multiplications per clock cycle and core; see Fig. 23(b). The dashed curves show the upper efficiency limit given by the available execution resources of each processor type, considering the assembler code of the dominating computational kernel.

APPENDIX B: ^{3}He

While the extrapolation results for ^{3}H were shown already in Sec. IV A, the corresponding results for ^{3}He energies (radii) are shown in Fig. 24 (Fig. 25).

The values for k_∞ resulting from the fit of Eq. (2) are shown in Fig. 26 and we find that a stable region is reached for large enough UV scales. The value in this stable region agrees very

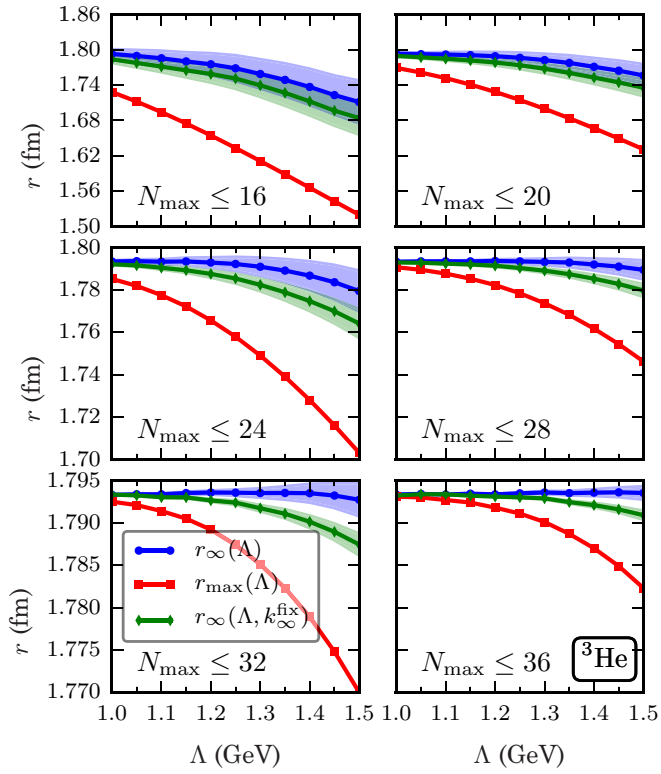

FIG. 25. Extrapolated ground-state (point-proton) radii $r_\infty(\Lambda)$ (circles) for ^{3}He. The different panels correspond to different NCSM model space truncations from $\max(N_{\max}) = 16$ to $\max(N_{\max}) = 36$. See caption of Fig. 5 for further details.

well with the ^{3}He separation momentum for $^3\text{He} \to d + p$, which is $k_\infty \approx 0.50$ fm^{-1}. We note that this momentum is not well separated from the momentum $k_{\rm sep}(^3\text{He} \to p + p + n) \approx 0.60$ fm^{-1} for three-body breakup.

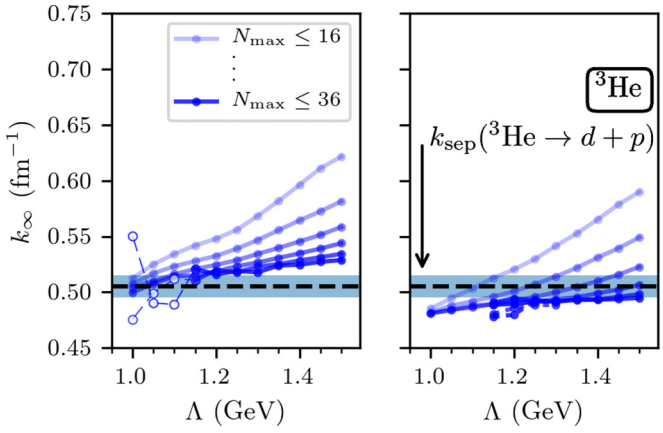

FIG. 26. Fit parameter $k_\infty(\Lambda)$ for ^{3}He energy extrapolation (left panel) and radius extrapolation (right panel) for different NCSM model space truncations from $\max(N_{\max}) = 16$ to $\max(N_{\max}) = 36$. Open symbols denote results for which UV corrections are expected to be larger than IR ones, and the corresponding fits are unreliable. The lowest, theoretical separation momentum is given as a dashed line with an uncertainty band.

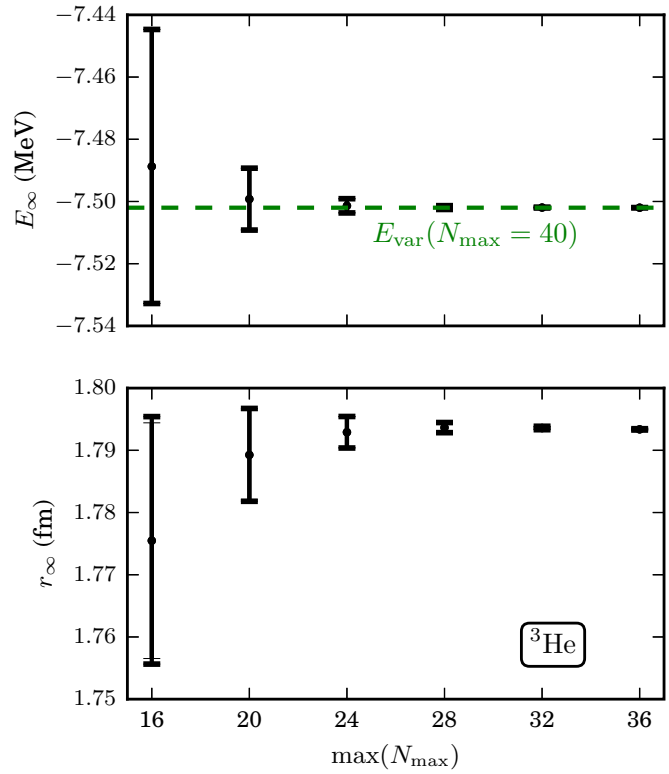

FIG. 27. Recommended results for the ^{3}He energy (upper panel) and radius (lower panel) for different NCSM model space truncations from $\max(N_{\max}) = 16$ to $\max(N_{\max}) = 36$.

Based on these observations we use the extrapolations at (fixed) $\Lambda = 1200$ MeV to extract a sequence of recommended results for the ground-state energy and the point-proton radius as a function of the model-space truncation; see Fig. 27. Overall, the quality of the results for ^{3}He is similar to those obtained for ^{3}H in Sec. IV A.

APPENDIX C: ASYMPTOTIC NORMALIZATION COEFFICIENT

We want relate the parameter a_0 of Eq. (2) to the asymptotic normalization coefficient. For the two-body system, the relation

$$a_0 = \frac{\hbar^2 k_\infty \gamma_\infty^2}{\mu} \tag{C1}$$

was derived in Ref. [30] using scattering theory. Here, μ is the reduced mass, k_∞ the canonical momentum corresponding to the two-particle distance $|\vec{r}_1 - \vec{r}_2|$, and γ_∞ the corresponding ANC. It is straightforward to derive the analogous expression for any two-body breakup. In the orthogonal Jacobi coordinates Eq. (12), this yields

$$a_0 = \frac{\hbar^2 k_\infty \gamma_\infty^2}{m}. \tag{C2}$$

For completeness, we also give a derivation of this result using the Hamiltonian. The derivation adapts the approaches of Lüscher [23] and König *et al.* [50] to our case.

Let ρ_1 be the orthogonal Jacobi coordinate that describes the separation between two clusters, and m the nucleon mass. Then the bound-state wave function of the two clusters is $\psi_{\rm sep}(\rho_1) = u_{\rm sep}(\rho_1)/\rho_1$, the separation energy is $E_{\rm sep} = -\hbar^2 k_{\rm sep}^2/(2m)$, and for interactions of range R, we have for $\rho_1 \gg R$

$$u_{\rm sep}(\rho_1) = \gamma_{\rm sep} e^{-k_{\rm sep}\rho_1}. \tag{C3}$$

Here the ANC ensures that the wave function is properly normalized. Let us consider the wave function

$$u(\rho_1) = \begin{cases} \alpha u_{\rm sep}(\rho_1), & \rho_1 < R, \\ \alpha \gamma_{\rm sep} e^{-k_{\rm sep}R} \frac{e^{-k_{\rm sep}\rho_1} - e^{-k_{\rm sep}(2L-\rho_1)}}{e^{-k_{\rm sep}R} - e^{-k_{\rm sep}(2L-R)}}, & R \leqslant \rho_1 \leqslant L. \end{cases}$$

Here, $u(\rho_1)$ is the exact finite-space wave function with separation energy $E_{\rm sep}$ of the Hamiltonian H for $R \leqslant \rho_1 \leqslant L$. We have $u(L) = 0$, since L is our hard-wall radius, and we assume $R \ll L$. Inspection shows that the normalization constant $\alpha = 1 + \mathcal{O}(k_{\rm sep} L e^{-2k_{\rm sep}L})$. We also have

$$\begin{aligned} u(R) &= \alpha \gamma_{\rm sep} e^{-k_{\rm sep}R}, \\ u'(R+\varepsilon) &= -k_{\rm sep} u(R) \coth(k_{\rm sep}[L-R]), \\ u'(R-\varepsilon) &= -k_{\rm sep} u(R), \end{aligned} \tag{C4}$$

where $\varepsilon \ll R$ is a small distance. We see that the wave function is continuous at $\rho_1 = R$, but its derivative makes a jump,

$$u'(R+\varepsilon) - u'(R-\varepsilon) \approx -2k_{\rm sep} e^{-2k_{\rm sep}(L-R)} u(R), \tag{C5}$$

at $\rho_1 = R$. Thus, $u(\rho_1)$ is an exact finite-space eigenfunction with energy $E_{\rm sep}$ of the Hamiltonian $H' = H + V$, with

$$V(\rho_1) = -\frac{\hbar^2 k_{\rm sep}}{m} e^{-2k_{\rm sep}(L-R)} \delta(\rho_1 - R). \tag{C6}$$

We note that V is exponentially small. Thus, $u(\rho_1)$ is an exponentially good approximation of the eigenfunction of H in a finite space. Let $u_L(\rho_1)$ denote the exact finite-space eigenstate of H, with eigenvalue E_L. We have

$$u_L(\rho_1) = \beta u(\rho_1) + \delta u(\rho_1), \tag{C7}$$

with $\beta = 1 + \mathcal{O}(e^{-k_{\rm sep}L})$ and $\delta u(\rho_1) = \mathcal{O}(e^{-k_{\rm sep}L})$, and $\langle u|\delta u\rangle = 0$. Thus,

$$\begin{aligned} \langle u_L|H|u\rangle &= \langle u_L|(H'-V)|u\rangle \\ &= E_{\rm sep}\langle u_L|u\rangle + \frac{\hbar^2 k_{\rm sep}}{m} e^{-2k_{\rm sep}L} u_L(R) u(R), \\ \langle u_L|H|u\rangle &= E_L \langle u_L|u\rangle, \end{aligned} \tag{C8}$$

from acting with H to the right and to the left, respectively. As $\langle u_L|u\rangle = 1 + \mathcal{O}(e^{-k_{\rm sep}L})$ and $u(R) \approx u_L(R) \approx u_{\rm sep}(R)$ up to exponentially small corrections, we get

$$E_L - E_{\rm sep} = \frac{\hbar^2 k_{\rm sep} \gamma_{\rm sep}^2}{m} e^{-2k_{\rm sep}L} \tag{C9}$$

in leading order. This is the desired result.

The generalization to many-body bound states and two-cluster breakup is straightforward, e.g., by following König and Lee [29]. In this case, the A-body wave function is the product

$$\Psi_A(\vec{r}_1, \ldots, \vec{r}_A) = \Psi_a(\vec{r}_1, \ldots, \vec{r}_a) \Psi_{A-a}(\vec{r}_{a+1}, \ldots, \vec{r}_A) \psi_{\rm sep}(\vec{\rho}_1). \tag{C10}$$

Here, ρ_1 denotes the orthogonal Jacobi coordinate between the clusters of a and $A-a$ particles, respectively. For ease of notation we suppressed the spin/isospin degrees of freedom, and it is also understood that the overall wave function Ψ_A needs to be properly antisymmetrized. The separation momentum is

$$k_{\rm sep} = \hbar^{-1} \sqrt{2m(B_A - B_a - B_{A-a})}, \tag{C11}$$

and B_n is the binding energy of the cluster with mass number n. We can now follow the derivation of Ref. [29] and arrive at the result Eq. (C9) for the correction to the separation energy.

In contrast to Ref. [29], the nucleon mass m (and not a reduced mass) enters the expression Eq. (C11), because we employ an orthogonal Jacobi coordinate ρ_1 instead of the physical separation,

$$\vec{r} \equiv \frac{1}{a} \sum_{i=1}^{a} \vec{r}_i - \frac{1}{A-a} \sum_{i=a+1}^{A} \vec{r}_i, \tag{C12}$$

of the center of masses between both clusters. Thus, our asymptotic normalization coefficient $\gamma_{\rm sep}$ needs to be rescaled before it can be compared to data. We have $\rho_1 = \sqrt{a(A-a)/A}|\vec{r}|$. Thus, our $k_{\rm sep}$ is the physical separation momentum times the factor $\sqrt{A/[a(A-a)]}$, and our ANC is the physical ANC times $(A/[a(A-a)])^{1/4}$.

[1] B. A. Brown and B. H. Wildenthal, Status of the nuclear shell model, Ann. Rev. Nucl. Part. Sci. **38**, 29 (1988).

[2] E. Caurier, G. Martínez-Pinedo, F. Nowacki, A. Poves, and A. P. Zuker, The shell model as a unified view of nuclear structure, Rev. Mod. Phys. **77**, 427 (2005).

[3] N. Shimizu, T. Abe, Y. Tsunoda, Y. Utsuno, T. Yoshida, T. Mizusaki, M. Honma, and T. Otsuka, New-generation Monte Carlo shell model for the K computer era, Prog. Theor. Exp. Phys. (2012) 01A205.

[4] N. Schunck, J. Dobaczewski, J. McDonnell, W. Satula, J. A. Sheikh, A. Staszczak, M. Stoitsov, and P. Toivanen, Solution of the Skyrme-Hartree-Fock-Bogolyubov equations in the Cartesian deformed harmonic-oscillator basis: (VII) HFODD (v2.49t): A new version of the program, Comp. Phys. Commun. **183**, 166 (2012).

[5] M. V. Stoitsov, N. Schunck, M. Kortelainen, N. Michel, H. Nam, E. Olsen, J. Sarich, and S. Wild, Axially deformed solution of the Skyrme-Hartree-Fock-Bogoliubov equations using the

transformed harmonic oscillator basis: (II) HFBTHO v2.00d: A new version of the program, Comp. Phys. Commun. **184**, 1592 (2013).
[6] T. Nikšić, N. Paar, D. Vretenar, and P. Ring, DIRHB—A relativistic self-consistent mean-field framework for atomic nuclei, Comp. Phys. Commun. **185**, 1808 (2014).
[7] P. Navrátil, S. Quaglioni, I. Stetcu, and B. R. Barrett, Recent developments in no-core shell-model calculations, J. Phys. G: Nucl. Part. Phys. **36**, 083101 (2009).
[8] B. R. Barrett, P. Navrátil, and J. P. Vary, *Ab initio* no core shell model, Prog. Part. Nucl. Phys. **69**, 131 (2013).
[9] W. H. Dickhoff and C. Barbieri, Self-consistent Green's function method for nuclei and nuclear matter, Prog. Part. Nucl. Phys. **52**, 377 (2004).
[10] G. Hagen, T. Papenbrock, M. Hjorth-Jensen, and D. J. Dean, Coupled-cluster computations of atomic nuclei, Rep. Prog. Phys. **77**, 096302 (2014).
[11] H. Hergert, S. K. Bogner, T. D. Morris, A. Schwenk, and K. Tsukiyama, The in-medium similarity renormalization group: A novel *ab initio* method for nuclei, Phys. Rep. **621**, 165 (2016).
[12] C. Forssén, G. Hagen, M. Hjorth-Jensen, W. Nazarewicz, and J. Rotureau, Living on the edge of stability, the limits of the nuclear landscape, Phys. Scr. **T152**, 014022 (2013).
[13] M. Horoi, A. Volya, and V. Zelevinsky, Chaotic Wave Functions and Exponential Convergence of Low-Lying Energy Eigenvalues, Phys. Rev. Lett. **82**, 2064 (1999).
[14] H. Zhan, A. Nogga, B. R. Barrett, J. P. Vary, and P. Navrátil, Extrapolation method for the no-core shell model, Phys. Rev. C **69**, 034302 (2004).
[15] G. Hagen, D. J. Dean, M. Hjorth-Jensen, T. Papenbrock, and A. Schwenk, Benchmark calculations for ^{3}H, ^{4}He, ^{16}O, and ^{40}Ca with *ab initio* coupled-cluster theory, Phys. Rev. C **76**, 044305 (2007).
[16] C. Forssén, J. P. Vary, E. Caurier, and P. Navrátil, Converging sequences in the *ab initio* no-core shell model, Phys. Rev. C **77**, 024301 (2008).
[17] S. K. Bogner, R. J. Furnstahl, P. Maris, R. J. Perry, A. Schwenk, and J. P. Vary, Convergence in the no-core shell model with low-momentum two-nucleon interactions, Nucl. Phys. A **801**, 21 (2008).
[18] I. Stetcu, B. R. Barrett, and U. van Kolck, No-core shell model in an effective-field-theory framework, Phys. Lett. B **653**, 358 (2007).
[19] G. Hagen, T. Papenbrock, D. J. Dean, and M. Hjorth-Jensen, *Ab initio* coupled-cluster approach to nuclear structure with modern nucleon-nucleon interactions, Phys. Rev. C **82**, 034330 (2010).
[20] E. D. Jurgenson, P. Navrátil, and R. J. Furnstahl, Evolving nuclear many-body forces with the similarity renormalization group, Phys. Rev. C **83**, 034301 (2011).
[21] S. A. Coon, M. I. Avetian, M. K. G. Kruse, U. van Kolck, P. Maris, and J. P. Vary, Convergence properties of *ab initio* calculations of light nuclei in a harmonic oscillator basis, Phys. Rev. C **86**, 054002 (2012).
[22] R. J. Furnstahl, G. Hagen, and T. Papenbrock, Corrections to nuclear energies and radii in finite oscillator spaces, Phys. Rev. C **86**, 031301 (2012).
[23] M. Lüscher, Volume dependence of the energy spectrum in massive quantum field theories. 1. Stable particle states, Commun. Math. Phys. **104**, 177 (1986).
[24] S. N. More, A. Ekström, R. J. Furnstahl, G. Hagen, and T. Papenbrock, Universal properties of infrared oscillator basis extrapolations, Phys. Rev. C **87**, 044326 (2013).
[25] R. J. Furnstahl, G. Hagen, T. Papenbrock, and K. A. Wendt, Infrared extrapolations for atomic nuclei, J. Phys. G: Nucl. Part. Phys. **42**, 034032 (2015).
[26] K. A. Wendt, C. Forssén, T. Papenbrock, and D. Sääf, Infrared length scale and extrapolations for the no-core shell model, Phys. Rev. C **91**, 061301 (2015).
[27] D. Odell, T. Papenbrock, and L. Platter, Infrared extrapolations of quadrupole moments and transitions, Phys. Rev. C **93**, 044331 (2016).
[28] B. Acharya, A. Ekström, D. Odell, T. Papenbrock, and L. Platter, Corrections to nucleon capture cross sections computed in truncated hilbert spaces, Phys. Rev. C **95**, 031301 (2017).
[29] S. König and D. Lee, Volume dependence of N-body bound states, Phys. Lett. B **779**, 9 (2018).
[30] R. J. Furnstahl, S. N. More, and T. Papenbrock, Systematic expansion for infrared oscillator basis extrapolations, Phys. Rev. C **89**, 044301 (2014).
[31] S. König, S. K. Bogner, R. J. Furnstahl, S. N. More, and T. Papenbrock, Ultraviolet extrapolations in finite oscillator bases, Phys. Rev. C **90**, 064007 (2014).
[32] A. M. Mukhamedzhanov and N. K. Timofeyuk, Astrophysical S factor for the reaction $^{7}\mathrm{Be} + p \rightarrow {}^{8}\mathrm{B} + \gamma$, JETP Lett. **51**, 282 (1990).
[33] P. Maris, J. P. Vary, and A. M. Shirokov, *Ab initio* no-core full configuration calculations of light nuclei, Phys. Rev. C **79**, 014308 (2009).
[34] R. G. Littlejohn, M. Cargo, T. Carrington, K. A. Mitchell, and B. Poirier, A general framework for discrete variable representation basis sets, J. Chem. Phys. **116**, 8691 (2002).
[35] A. Ekström, G. Baardsen, C. Forssén, G. Hagen, M. Hjorth-Jensen, G. R. Jansen, R. Machleidt, W. Nazarewicz, T. Papenbrock, J. Sarich, and S. M. Wild, Optimized Chiral Nucleon-Nucleon Interaction at Next-to-Next-to-Leading Order, Phys. Rev. Lett. **110**, 192502 (2013).
[36] Top500 supercomputer sites, https://www.top500.org/lists/2017/11/ (2017).
[37] C. W. Johnson, W. E. Ormand, and P. G. Krastev, Factorization in large-scale many-body calculations, Comput. Phys. Commun. **184**, 2761 (2013).
[38] E. Caurier and F. Nowacki, Present status of shell model techniques, Act. Phys. Pol. B **30**, 705 (1999).
[39] E. Caurier, G. Martínez-Pinedo, F. Nowacki, A. Poves, J. Retamosa, and A. P. Zuker, Full $0\hbar\omega$ shell model calculation of the binding energies of the $1f_{7/2}$ nuclei, Phys. Rev. C **59**, 2033 (1999).
[40] P. Navrátil and E. Caurier, Nuclear structure with accurate chiral perturbation theory nucleon-nucleon potential: Application to ^{6}Li and ^{10}B, Phys. Rev. C **69**, 014311 (2004).
[41] I. J. Shin, Y. Kim, P. Maris, J. P. Vary, C. Forssén, J. Rotureau, and N. Michel, *Ab initio* no-core solutions for ^{6}Li, J. Phys. G **44**, 075103 (2017).
[42] Y. E. Kim and A. Tubis, The theory of three-nucleon systems, Annu. Rev. Nucl. Sci. **24**, 69 (1974).
[43] B. A. Girard and M. G. Fuda, Asymptotic normalization parameter of the triton, Phys. Rev. C **19**, 583 (1979).
[44] M. A. Caprio, P. Maris, and J. P. Vary, Coulomb-sturmian basis for the nuclear many-body problem, Phys. Rev. C **86**, 034312 (2012).

[45] R. Sánchez, W. Nörtershäuser, G. Ewald, D. Albers, J. Behr, P. Bricault, B. A. Bushaw, A. Dax, J. Dilling, M. Dombsky, G. W. F. Drake, S. Götte, R. Kirchner, H.-J. Kluge, Th. Kühl, J. Lassen, C. D. P. Levy, M. R. Pearson, E. J. Prime, V. Ryjkov, A. Wojtaszek, Z.-C. Yan, and C. Zimmermann, Nuclear Charge Radii of ^{9,11}Li: The Influence of Halo Neutrons, Phys. Rev. Lett. **96**, 033002 (2006).

[46] B. S. Pudliner, V. R. Pandharipande, J. Carlson, S. C. Pieper, and R. B. Wiringa, Quantum Monte Carlo calculations of nuclei with $A < 7$, Phys. Rev. C **56**, 1720 (1997).

[47] T. Dytrych, A. C. Hayes, K. D. Launey, J. P. Draayer, P. Maris, J. P. Vary, D. Langr, and T. Oberhuber, Electron-scattering form factors for ^{6}Li in the *ab initio* symmetry-guided framework, Phys. Rev. C **91**, 024326 (2015).

[48] H. Kümmel, K. H. Lührmann, and J. G. Zabolitzky, Many-fermion theory in expS- (or coupled cluster) form, Phys. Rep. **36**, 1 (1978).

[49] A. G. Taube and R. J. Bartlett, Improving upon CCSD(T): Λ CCSD(T). I. Potential energy surfaces, J. Chem. Phys. **128**, 044110 (2008).

[50] S. König, D. Lee, and H.-W. Hammer, Non-relativistic bound states in a finite volume, Ann. Phys. **327**, 1450 (2012).